MASTER THESIS

Jan Priessnitz

Modeling and study of quasi-two-dimensional magnetic materials

Department of Condensed Matter Physics

Prague 2023

I declare that I carried out this master thesis independently, and only with the cited sources, literature and other professional sources. It has not been used to obtain another or the same degree.

I understand that my work relates to the rights and obligations under the Act No. 121/2000 Sb., the Copyright Act, as amended, in particular the fact that the Charles University has the right to conclude a license agreement on the use of this work as a school work pursuant to Section 60 subsection 1 of the Copyright Act.

In . . . . date . . . .
                                                                              Author's signature

Title: Modeling and study of quasi-two-dimensional magnetic materials

Author: Jan Priessnitz

Department: Department of Condensed Matter Physics

Supervisor: RNDr. Pavel Baláž, Ph. D., FZU - Institute of Physics of the Czech Academy of Sciences

Abstract: Dzyaloshinskii-Moriya interaction (DMI) is a type of exchange interaction found in non-centrosymmetric structures. It favors spin canting, and it is an important mechanism for stabilizing non-collinear magnetic structures, such as skyrmions, which are promising candidates for applications in spintronics. Furthermore, DMI plays a significant role in multiferroics and can support magnetoelectricity. Both phenomena are often observed in layered materials.

This thesis explores, through numerical simulations, the effect of out-of-plane DMI on magnetic ordering in two-dimensional triangular lattices. It uses the classical Heisenberg model together with Markov Chain Monte Carlo and spin dynamics simulation methods. Apart from DMI, the Hamiltonian includes ferromagnetic exchange interaction between nearest neighbours and interaction with external magnetic field.

In the first part, the zero-temperature properties of the system are computed for various DMI strengths and external magnetic fields, and a phase diagram is constructed. Three magnetic phases are observed: ferromagnetic, antiferromagnetic cycloidal, and conical – a mixture of the former two.

The second part focuses on finite-temperature properties, starting with specific heat capacity, magnetization, and magnetic susceptibility. DMI does not affect the critical ordering temperature but enhances magnetization at higher temperatures below the critical temperature. It was shown that DMI favours magnetization in the z-direction in the ferromagnetic phase. Next, finite-temperature hysteresis loops are presented. Anomalous hysteresis in the ferromagnetic phase induced by DMI and temperature is observed, resulting in non-zero coercivity increasing with DMI strength and temperature. The coercivity is associated with the DMI energy barrier and a possible explanation is outlined – traces of antiferromagnetic order were observed in the otherwise ferromagnetic phase at higher temperatures.

Keywords: Dzyaloshinskii-Moriya, classical Heisenberg model, atomistic spin dynamics, Monte Carlo, magnetic order

Contents

Introduction

In recent years, magnetism has become a more and more popular topic of study amongst solid-state physicists and despite this, there are still many magnetic phenomena not yet fully understood and many yet to be explored.

Take, for example, the giant magnetoresistance effect, where the electric resistance of a layered sample significantly depends on the orientation of individual ferromagnetic layers. This phenomenon was deemed so important that the 2007 Nobel Prize in Physics was awarded to its discoverers, Albert Fert and Peter Grünberg. Indeed the giant magnetoresistance effect has drastically improved the storage capacity in hard drives, a very important application.

The giant magnetoresistance effect is just one of many couplings between magnetism and other physical properties. Other similar effects can be observed in materials called multiferroics, which are materials that exhibit multiple ferroic properties in the same phase: a combination of ferromagnetism, ferroelectricity, and ferroelasticity. An example of this is the magnetoelectric effect – a sample becomes magnetized in an electric field, or becomes electrically polarized in a magnetic field. Dzyaloshinskii-Moriya exchange interaction (DMI) has been found to play an important role in magnetoelectricity (Sergienko and Dagotto [2006]) because it is coupled to displacement of some atoms in the lattice. This is in turn coupled with electric polarization.

DMI is essential in one other area of interest: spintronics. Spintronics is a branch of solid-state physics which studies behaviour of electronic spin in solid-state devices. It has been shown that DMI stabilizes magnetic skyrmions (Muehlbauer et al. [2009]), topologically stable magnetic textures made of spin vortices. Skyrmions are currently researched for application as a computer memory storage device (Fert et al. [2013]) or in neuromorphic computing (Song et al. [2020]), because they are topologically stable, but they can be manipulated using spin currents, potentially providing a more energy efficient alternative to present computers based on charge current. Ultrathin magnetic films are often picked for this purpose. Magnetic ordering in these films can be modeled on a two-dimensional lattice.

In this thesis, we explore the role of DMI in one particular configuration: on a two-dimensional triangular lattice together with ferromagnetic direct exchange interaction, external magnetic field, and with DMI vector pointing out of plane. We use classical Heisenberg model with Monte Carlo Markov Chain and spin dynamics (Landau-Lifshitz-Gilbert equation) methods. In the first part, we investigate the zero-temperature magnetic ordering for various DMI and external magnetic field strengths and construct a phase diagram. In the second part, we calculate temperature dependence of specific heat capacity, magnetization, and susceptibility to determine the critical ordering temperature T_c. We also calculate the hysteresis loops for various DMI strength and temperatures, observing anomalous ferromagnetic hysteresis induced by DMI and temperature.

The model was choosed based on the structure of $EuAl_{12}O_{19}$ – a triangular ferromagnetic compound experimentally investigated by Gaël Bastien, Ph. D. [1].

---

[1]Charles University, Faculty of Mathematics and Physics, Department of Condensed Matter Physics, Prague, Czech Republic

1. Theory

1.1 Magnetism in solid-state materials

The particles responsible for magnetism in solids are electrons. The magnetic moment of a single electron has two sources: spin angular momentum and orbital angular momentum.

$$\vec{\mu_S} = g_S \frac{e}{2m_e} \vec{S} = g_S \frac{\mu_B}{\hbar} \vec{S}$$
$$\vec{\mu_L} = \frac{e}{2m_e} \vec{L} = \frac{\mu_B}{\hbar} \vec{L}$$

(1.1)

where $g_S \approx 2.0023$ is the spin g-factor, m_e is electron mass, μ_B is the Bohr magneton, $\vec{L}$ is the electron orbital angular momentum and $\vec{S}$ is the spin angular momentum. Magnitudes of the magnetic moments are linked to the spin quantum number $s = 1/2$ and orbital quantum number $l = 0, 1, 2, ..., n$:

$$|\vec{\mu_S}| = g_S \mu_B \sqrt{s(s+1)}$$
$$|\vec{\mu_L}| = \mu_B \sqrt{l(l+1)}$$

(1.2)

Magnetism in solids is further classified as itinerant or localized, depending on the state of the electrons responsible for it.

Itinerant magnetism

Itinerant magnetism arises from the band electrons and spontaneous spin-dependent band splitting, caused by the repulsive Coulomb interaction (arising from the Pauli exclusion principle). In this case, the half-filled band near the Fermi level splits into distinct spin-up and spin-down bands. Electrons move from one band to the other, causing uneven band filling and occupying states with higher energy. However, the total energy is lower, due to the weakened repulsive Coulomb interaction. The condition for the band splitting is called the Stoner criterion

$$D(E_F) \cdot U > 1$$

(1.3)

where $D(E_F)$ is the density of states at Fermi level and U is the strength of the repulsive Coulomb interaction.

Localized magnetism

On the other hand, localized magnetism, as the name suggests, comes from localized electrons orbiting a single atom. The magnetic dipole moment of one whole atom is a sum of magnetic dipole moments of all its electrons. This means that lower, fully occupied shells do not contribute to magnetism, since individual angular momentum contributions cancel out. Only half-occupied shells have a non-zero contribution to the atomic magnetic dipole moment. Localized magnetism most commonly appears in half-filled $4f$ shells of rare-earth compounds. The total magnetic dipole moment depends on the electron configuration in the outermost

shell. Each electron state is identified by spin quantum number $m_S = \pm 1/2$ and orbital quantum number $m_L = \pm 0, \pm 1, .., \pm l$ so that there is a total of $2(2l+1)$ electron states in one shell. A concrete electron configuration yields total spin angular momentum number $S = \sum m_S$, total orbital angular momentum number $L = \sum m_L$, and total angular momentum number $J = L + S$. Hund's rules determine the ground state electron configuration and resulting S, L, J:

1. Configuration with largest possible S has the lowest energy.

2. From the configurations permitted by the first rule, configuration with the largest possible L has the lowest energy.

3. From configurations permitted by the rules above, configuration with $J = |L - S|$ or $J = |L + S|$, respectively for less or more than half-filled shells, has the lowest energy.

The first two rules come from the Pauli exclusion principle and the repulsive Coulomb interaction. The last rule comes from the spin-orbit interaction, which couples the direction of $\vec{\mu_S}$ and $\vec{\mu_L}$. Effective magnetic moment of the atom is then

$$|\vec{\mu_{\text{eff}}}| = g_J \mu_B \sqrt{J(J+1)} \tag{1.4}$$

where g_J is the Landé g-factor.

1.2 Magnetic interactions

In the previous section, we described the microscopic magnetic dipole moment carried by one atom. What happens when there are multiple magnetic atoms nearby? Several types of exchange interactions, mediated by the electrons, are present. These interactions are the prerequisites for macroscopic magnetic behaviour which is introduced in section 1.3.

1.2.1 Direct exchange

We start with a simple model – a hydrogen molecule with two orthogonal $1s$ states φ_1 and φ_2 and one electron (Pavarini et al. [2012]). We begin with a simplified scenario, where the two electrons behave independently and do not interact. Both protons have one orbital function: ϕ_1, ϕ_2, and they are orthogonal. φ_1 and φ_2 form the basis of the system. The hopping element is

$$-t = \langle \varphi_1 | \hat{H} | \varphi_2 \rangle = \int \mathrm{d}r^3 \varphi_1^*(\vec{r}) \left[-\frac{\hbar^2}{2m_e} \nabla^2 + U(\vec{r}) \right] \varphi_2(\vec{r}) \tag{1.5}$$

resulting in Hamiltonian matrix

$$H = \begin{pmatrix} 0 & -t \\ -t & 0 \end{pmatrix} \tag{1.6}$$

Diagonalization of H yields two eigenstates

$$\varphi_\pm = \frac{1}{\sqrt{2}} (\varphi_1 \pm \varphi_2) \tag{1.7}$$

with energies $\epsilon_\pm = \mp t$.

We will denote a spin-up electron in orbital φ_1 as $|\uparrow, \cdot\rangle$. Let us now have 2 electrons with opposite spins. The basis consists of four states: $|\uparrow, \downarrow\rangle$, $|\downarrow, \uparrow\rangle$, $|\uparrow\downarrow, \cdot\rangle$, $|\cdot, \uparrow\downarrow\rangle$.

$$
H = \begin{pmatrix} 0 & 0 & -t & -t \\ 0 & 0 & +t & +t \\ -t & +t & U & 0 \\ -t & +t & 0 & U \end{pmatrix} \begin{matrix} |\uparrow, \downarrow\rangle \\ |\downarrow, \uparrow\rangle \\ |\uparrow\downarrow, \cdot\rangle \\ |\cdot, \uparrow\downarrow\rangle \end{matrix} \tag{1.8}
$$

In $|\uparrow\downarrow, \cdot\rangle$ and $|\cdot, \uparrow\downarrow\rangle$ states, two electrons share one orbital and are subject to the repulsive Coulomb interaction U. The electron hopping results in the off-diagonal elements $\pm t$, where the sign change is related to electron order change and Fermi statistic.

Diagonalization of the matrix above yields the following eigenstates:

$$
\Psi_\pm = \frac{|\uparrow, \downarrow\rangle - |\downarrow, \uparrow\rangle - \frac{\epsilon_\pm}{2t}(|\uparrow\downarrow, \cdot\rangle + |\cdot, \uparrow\downarrow\rangle)}{\sqrt{2 + \epsilon_\pm^2/(2t^2)}} \qquad \epsilon_\pm = \frac{U}{2} \pm \frac{\sqrt{U^2 + 16t^2}}{2}
$$

$$
\Psi_{\text{cov}} = \frac{1}{\sqrt{2}}(|\uparrow, \downarrow\rangle + |\downarrow, \uparrow\rangle) \qquad \epsilon_{\text{cov}} = 0 \tag{1.9}
$$

$$
\Psi_{\text{ion}} = \frac{1}{\sqrt{2}}(|\uparrow\downarrow, \cdot\rangle - |\cdot, \uparrow\downarrow\rangle) \qquad \epsilon_{\text{ion}} = U
$$

Now we assume that U is far larger than t and work with the limit of $U \to \infty$. In that case, energy of states Ψ_+ and Ψ_{ion} is very large and these states can be neglected. Remaining are states Ψ_{cov} and Ψ_-. Energy of Ψ_- can be expanded to $\epsilon_- = -4t^2/U$. Assuming that both t and U are positive, Ψ_- is the ground state of a system with spin-up and spin-down electron.

In the case of same-spin electrons, the ground states are $|\uparrow, \uparrow\rangle$ or $|\downarrow, \downarrow\rangle$ with energy $\epsilon = 0$ – electron hopping is forbidden and no energy decrease is happening.

From here, we can construct the effective Hamiltonian. Let us denote the exchange interaction energy as $J = 4t^2/U$ and electron spin operators $\hat{S}_1$ and $\hat{S}_2$. The value of product $\hat{S}_1 \cdot \hat{S}_2$ is $1/4$ for parallel spins and $-3/4$ for antiparallel spin (Ashcroft and Mermin [2011]). The effective Hamiltonian satisfying the condition is

$$
H = J\left(\vec{S}_1 \cdot \vec{S}_2 - \frac{1}{4}\right) \tag{1.10}
$$

Since J is positive in this case, direct exchange interaction favours antiparallel (antiferromagnetic) orientation of neighbouring spins.

1.2.2 Superexchange

Superexchange is an interaction between two magnetic atoms working on a principle similar to direct exchange. It can explain antiferromagnetism in transition-metal oxides, where the magnetic atoms are too far apart for direct exchange interaction (Pavarini et al. [2012]). In this case, the exchange is mediated by a

non-magnetic atom located in the middle of the two magnetic atoms. An example of such a compound is MnO with Mn-O-Mn bonds, where d-orbitals in manganese and p-orbital in oxygen participate in the interaction.
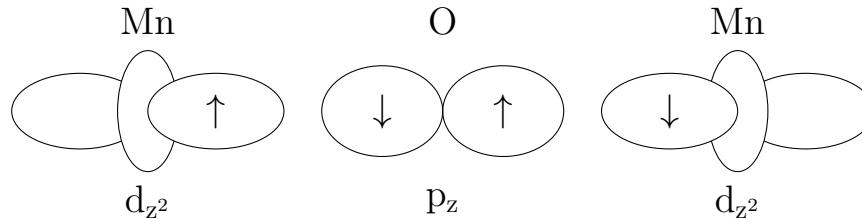
The state with antiparallel spins on Mn atoms has lower energy, because it allows additional electron hopping processes, while parallel spins do not. The effective Hamiltonian is

$$H = \frac{t_{\text{Mn,O}}^2}{U} \vec{S}_1 \cdot \vec{S}_2 \tag{1.11}$$

1.2.3 Double exchange

Double exchange shares a similarity with superexchange – it is also an exchange between two magnetic atoms mediated by a central non-magnetic atom. But in this case, the magnetic atoms need to be in different oxidation states. This happens in systems with a non-integral number of electrons per site caused by conduction electrons moving around the system. Again, we will demonstrate the interaction on the Mn-O-Mn system. The difference from superexchange lies in the oxidation states of manganese atoms Mn^{3+} and Mn^{4+}. Here, the conduction electron hopping from atom Mn^{3+} to Mn^{4+}, while retaining the original spin, is most favourable when the remaining electrons in both d-orbitals are parallel. This follows from the repulsive Coulomb interaction and first Hund's rule – the conduction electron must be parallel to the rest of d-shell electrons both before and after the hopping. For this reason, the double exchange interaction favours parallel (ferromagnetic) ordering of the spins. The exchange interaction term in effective Hamiltonian has negative coefficient $-J$:

$$H = -J\vec{S}_1 \cdot \vec{S}_2 \quad , \quad J > 0 \tag{1.12}$$

1.2.4 Dzyaloshinskii-Moriya interaction

Dzyaloshinskii-Moriya interaction (DMI), or antisymmetric interaction, is the antisymmetric part of anisotropic superexchange. It originates from spin-orbit coupling and is only present in lattices with broken inversion symmetry. The effective Hamiltonian for DMI is

$$H = \vec{D} \cdot (\vec{S}_1 \times \vec{S}_2) \tag{1.13}$$

DMI favours spin canting in otherwise antiferromagnetic structures and explains weak ferromagnetism (Moriya [1960]).

Furthermore, it is considered one of the most important interactions for specific chiral textures such as magnetic skyrmions (Ham et al. [2021]).

The direction of DMI vector is to some extent dictated by the lattice symmetry (Moriya [1960]). Let us denote locations of magnetic ions as A and B and point bisecting AB as C. The rules for DMI vector $\vec{D}$ are:

- When a center of inversion is located at C, $\vec{D} = \vec{0}$.

- When a mirror plane perpendicular to AB passes through C, $\vec{D}$ is parallel to that mirror plane and perpendicular to AB.

- When there is a mirror plane including A and B, $\vec{D}$ is perpendicular to that mirror plane.

- When a two-fold rotation axis perpendicular to AB passes through C, $\vec{D}$ is perpendicular to that axis.

- When there is an n-fold axis ($n \geq 2$) along AB, $\vec{D}$ is parallel to that axis.

1.2.5 Magnetic dipole interaction

Every magnetic atom has a non-zero magnetic dipole moment, so a classical dipole-dipole interaction is also present in magnetic compounds. The Hamiltonian of this interaction is

$$H = -\frac{\mu_0}{4\pi|\vec{r}|^3} \left(3(\vec{m}_1 \cdot \vec{r})(\vec{m}_2 \cdot \vec{r}) - \vec{m}_1 \cdot \vec{m}_2 \right) \tag{1.14}$$

where $\vec{m}_1$ and $\vec{m}_2$ are the magnetic dipole moments and $\vec{r}$ is their relative position. In most solids, this interaction has energy in the order of 10^{-4} eV, while the other exchange interactions usually have energies of a fraction of eV (Ashcroft and Mermin [2011]). Magnetic dipole-dipole interaction is therefore neglected in this thesis.

1.3 Magnetic ordering

Now, let us move to a larger scale and imagine an infinite lattice of magnetic atoms (or sites). So far, we have established that some compounds are made of magnetic atoms possessing a non-zero magnetic dipole moment. The moments themselves are microscopical and as long as they are arranged randomly, they do not amount to any macroscopic magnetization. We have also introduced exchange interactions between the magnetic dipole moments which couple their directions. They result in macroscopic-scale magnetic ordering, which results in non-zero macroscopic magnetization.

In this section, we will go through possible magnetic orderings and their behaviour in finite temperatures.

Ferromagnetic ordering

Ferromagnetic ordering arises when neighbouring spins prefer parallel orientation. This results in a situation when all spins in the lattice are oriented in the same direction. The magnetization of such ordering is

$$M = \frac{\mu_{\text{eff}}}{V} \tag{1.15}$$

where μ_{eff} is the magnetic dipole moment of one site and V is the unit cell volume.

Antiferromagnetic ordering

Antiferromagnetic ordering occurs when the exchange interaction between neighbouring magnetic atoms favours antiparallel spin orientation. The magnetization of antiferromagnetic ordering is $M = 0$. Depending on the lattice symmetry, we can observe more complicated orderings, such as:

- amplitude-modulated ordering – magnetic dipole moment magnitude and direction oscillates between $-\mu_{\text{eff}}$, μ_{eff} along one spatial direction, moments with $|\mu| < \mu_{\text{eff}}$ are permitted

- spiral ordering - magnetic moments rotate around an axis parallel to the direction of propagation

- cycloidal ordering - magnetic moments rotate around an axis perpendicular to the direction of propagation

There is another type called conical ordering – magnetic moments rotate around a conus with axis perpendicular to the direction of propagation. The ordering is antiferromagnetic in the plane of propagation but has a non-zero magnetization in the direction of the axis.

Note that another kind of ordering with non-zero magnetization, called uncompensated antiferromagnetic, or ferrimagnetic, exists. It requires multiple kinds of magnetic atoms with different magnetic dipole moments and it does not appear in this thesis.

Propagation vector

Propagation vector $\vec{k}$ further describes magnetic ordering. It expresses the relationship between a chemical unit cell of the compound and a magnetic unit cell. A magnetic unit cell is an analogy to an ordinary (chemical) unit cell, but also with the magnetic moments placed on the magnetic atoms. The magnetic unit cell is either the same or larger than the chemical unit cell. It contains an integral number of chemical unit cells and it is the smallest possible cell fulfilling the translational symmetry of both the atoms and the magnetic moments.
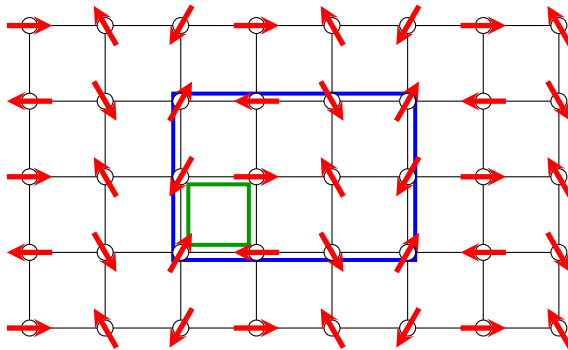
We demonstrate this on an example 2D lattice.

Figure 1.1: 2D lattice with magnetic moments. The magnetic unit cell (blue) consists of 3×2 chemical unit cells (green). Antiferromagnetic cycloidal ordering.

Figure 1.1 shows an example magnetic unit cell containing $X \times Y = 3 \times 2$ chemical unit cells. The propagation vector is then calculated as $\vec{k} = (1/X, 1/Y)$ (or $\vec{k} = (1/X, 1/Y, 1/Z)$ in 3D lattices). In this case $\vec{k} = (1/3, 1/2)$. Note that ferromagnetic structures are conventionally described by a propagation vector $\vec{k} = (0, 0)$.

Temperature dependence

The situation described above, where the spins are precisely ordered, only happens for zero temperature. Temperature, which disorders the spins, competes with the exchange interactions. For a ferromagnetic system, this means decreasing magnetization as the temperature increases. At critical temperature T_c (called Curie temperature for ferromagnetic and Néel temperature for antiferromagnetic orderings), the system undergoes a second-order phase transition. The system loses the magnetic ordering for temperatures higher than T_c and becomes paramagnetic.

Mean field approximation provides expressions for magnetization in both ferromagnetic and paramagnetic states. In the paramagnetic state, the defining quantity is the paramagnetic susceptibility determined by the Curie-Weiss law $\chi = C/(T - T_c)$, where C is the Curie constant. In the ferromagnetic state, magnetization is determined by the Brillouin expression $m = \tanh{(m/t)}$, where m is reduced magnetization and t is reduced temperature ($t = 1$ is critical temperature). Note that mean-field approximation does not give a good result in low temperatures, where magnetization follows Bloch law $M(T) = M(0)(1 - (T/T_c)^{3/2})$.

The magnetic order (or disorder) contributes to entropy and the magnetic moment disordering contributes to the specific heat capacity of the system. Indeed, one can calculate specific heat capacity of the magnetic system in the classical Heisenberg model simulation. The (anti-)ferromagnetic/paramagnetic second-order phase transition is connected to a peak in specific heat capacity.

Determining the critical temperature solely based on specific heat is inaccurate, because of the limited size of the simulated lattice. Binder cumulant is a useful quantity for overcoming this problem and determining the phase transition temperature accurately (Landau and Binder [2009]). In the context of magnetism, it is calculated using magnetization as

$$U_L = 1 - \frac{\langle M^4 \rangle_L}{3 \langle M^2 \rangle_L^2} \tag{1.16}$$

where $\langle ... \rangle_L$ denotes averaging over the statistical ensemble measured for specific temperature and lattice size L. The critical temperature is the point where U_L curves for different lattice sizes cross.

1.4 Classical Heisenberg model

The classical Heisenberg model is used to describe the behaviour of magnetic moments in a lattice. As the name suggests, it neglects quantum effects, making it unsuitable for certain classes of materials, like antiferromagnets, where the quantum effects are significant and the ground state is a mixed quantum state unreachable by the classical model.

It works on a lattice of 3D fixed-magnitude spin vectors $\vec{S}_i \in \mathbb{R}^3, |\vec{S}_i| = 1$, representing the localized magnetic dipole moments. The Hamiltonian can include various interactions amongst the spins or with external field. Direct exchange, superexchange, double exchange, or others are specified only by $J_{ij} \in \mathbb{R}$ which specifies the interaction energy between $\vec{S}_i$ and $\vec{S}_j$. DMI is defined by DMI vectors $D_{ij} \in \mathbb{R}^3$. Interaction with external field depends on the local magnetic field strength $\vec{h}_i$ and the magnetic dipole moment of the spin μ_i.

$$\mathcal{H} = -\sum_{ij} J_{ij} \vec{S}_i \cdot \vec{S}_j - \sum_{ij} \vec{D}_{ij} \cdot (\vec{S}_i \times \vec{S}_j) - \sum_i \mu_0 \mu_i \vec{h}_i \cdot \vec{S}_i \qquad (1.17)$$

This is the general form of the classical Heisenberg model Hamiltonian. Note that other types of interactions can also be included, like anisotropic exchange interaction, biquadratic interaction, or magnetocrystalline anisotropy. However, the general form is rarely used in practice. An example of a simplified Hamiltonian is

$$\mathcal{H} = -\sum_{\langle ij \rangle} J \vec{S}_i \cdot \vec{S}_j - \sum_{\langle ij \rangle} \vec{D}_{ij} \cdot (\vec{S}_i \times \vec{S}_j) - \sum_i \vec{H} \cdot \vec{S}_i \qquad (1.18)$$

where $\langle ij \rangle$ denotes summing of all nearest neighbour pairs. We can see several simplifications: exchange interaction is considered only between nearest neighbours with constant global interaction energy J. The same applies for DMI, although the DMI vector $\vec{D}_{ij}$ usually depends on the relative position of $\vec{S}_i$ and $\vec{S}_j$. All spins have the same magnetic dipole moment $\mu_0 \mu_i = 1$ and the external field is homogeneous $\vec{h}_i = \vec{H}$.

1.5 Markov Chain Monte Carlo

Almost all calculations in this thesis are based on searching either for a ground state of a specific Hamiltonian or for thermal average of states within a certain temperature. The state space for the Heisenberg model is infinite because there is an infinite number of unique unit vectors in three-dimensional space. We could discretize the unit vector space into N states (a unit vector $\vec{S}_i$ is in 1 out of N states), but for a Heisenberg model with $L \times L$ spins, the state space is far too large (number of states is N^{L^2}) to iterate over all states in a reasonable time. We need a better method to search for the ground state.

Stochastic algorithms based on the Markov Chain Monte Carlo (MCMC) method have proven useful for finding approximate solutions to problems based on the classical Heisenberg model in a reasonable time. Mathematically speaking, the MCMC method aims to accurately sample given probability distribution. In our case, we want to sample the Boltzmann distribution of the system, where the lowest-energy states are the most probable. This suits our goal of searching for the ground state.

Markov Chains

Markov chain is a useful mathematical formalism to model a wide class of stochastic processes. In this thesis, we use Markov chains to sample the Boltzmann

distribution of the system, since constructing this distribution explicitly is impossible due to the infinite state space. Here, we present a simple definition of Markov chains inspired by Chan et al. [2012].

Markov chain is a sequence of random variables $S_0, S_1, S_2, ..., S_k, S_{k+1}, ...$, such that

1. Each variable takes a value from the state space $S_k \in S$, $S = 0, 1, 2, ...$.

2. Conditional probability fulfills condition
   $P(S_{k+1} = j | S_k = i_k, S_{k-1} = i_{k-1}, S_0 = i_0) = P(S_{k+1} = j | S_k = i_k)$. In other words, the probability of transition $P(S_{k+1} = j | S_k = i_k)$ does not depend on the history of the process.

3. $P(S_{k+1} = j | S_k = i) = p_{ij}$, which does not depend on k.

The transition probability $p_{ij} \in \langle 0, 1 \rangle$ needs to be defined for each pair of states i and j. For finite state spaces, p_{ij} is often written as a matrix. For infinite state spaces, it is a general function $p(i, j) \in \langle 0, 1 \rangle$.

We require that the modeled distribution $P(S)$ is stationary and does not depend on k. This is guaranteed by the detailed balance condition (Loison et al. [2004]):

$$P(S = i) \cdot p_{ij} = P(S = j) \cdot p_{ji} \tag{1.19}$$

Metropolis-Hastings algorithm

Metropolis-Hastings algorithm is a Markov Chain Monte Carlo method designed to solve the problem of sampling from a Boltzmann distribution.

It uses Markov chains to draw random samples from a distribution of states. The distribution does not need to be described explicitly, but rather as a Markov Chain transition probability function. This is very convenient because it allows us to easily describe a state distribution that would be difficult to define explicitly.

Let us have the Heisenberg model of $L \times L$ spin lattice. A state X_k consists of L^2 spin vectors $X_k = (\vec{S}_1, \vec{S}_2, ..., \vec{S}_{L \times L})$. The state distribution is defined via transition probability function $p(X_i, X_j) \in \langle 0, 1 \rangle$. Initial state X_0 is selected randomly or based on specific initial conditions. Markov Chain Monte Carlo draws samples $X_1, X_2, ...$ from the state space based on following scheme:

1. site $i \in 1, 2, ..., L^2$ is randomly selected

2. random new state X_{prop} based on current state X_k is proposed, such that only the i-th spin is modified: $X_{\text{prop}} = (\vec{S}_1^k, \vec{S}_2^k, ..., \vec{S}_i^{\text{prop}}, ..., \vec{S}_{L \times L}^k)$

3. number p' is randomly generated from uniform distribution $\langle 0, 1 \rangle$

4. $X_{k+1} = X_{\text{prop}}$ (proposed state is accepted) if $p' < p(X_k, X_{\text{prop}})$, otherwise $X_{k+1} = X_k$ (proposed state is rejected)

The beauty of this method is in the simplicity of the transition probability function $p(X_i, X_j)$, which depends only on the energy of states E_i and E_j, and current temperature T.

$$p(i,j) = \begin{cases} \exp\left(-\frac{E_j - E_i}{k_b T}\right) & E_j > E_i \\ 1 & E_j \leq E_i \end{cases} \tag{1.20}$$

The proposed spin vector $\vec{S}_i^{\text{prop}}$ is usually generated reasonably close to the original spin vector, such that $\vec{S}_i^{\text{prop}} \cdot \vec{S}_i^k \to 1$. The choice of the new spin vector affects the speed of convergence of the method. If almost all proposed states are accepted, the spin vector modifications are too small. On the other hand, if almost all proposed states are rejected, the algorithm rarely updates the state. A proposal acceptance rate of 0.5 is optimal with respect to the speed of convergence (Becca and Sorella [2017]).

Heat Bath

Heat bath is another Markov Chain Monte Carlo method, an alternative to the Metropolis-Hastings algorithm. The principle of heat bath is that all interactions in the Hamiltonian can be expressed in the form of an effective field $\vec{H}_i$ acting on spin $\vec{S}_i$. For each spin $\vec{S}_i$, a Boltzmann probability distribution can be defined, telling us what is the probability of finding a spin in a certain direction at temperature T. This probability distribution is then directly sampled and the spin direction is updated.

We follow the scheme proposed by Miyatake et al. [1986]. We start with rearranging the Hamiltonian to express the local effective field

$$\mathcal{H} = -J \sum_{<ij>} \vec{S}_i \cdot \vec{S}_j - \sum_{<ij>} \vec{D}_{ij} \cdot (\vec{S}_i \times \vec{S}_j) - \vec{H} \cdot \left(\sum_i \vec{S}_i\right) =$$

$$= -\sum_i \left[\sum_{i<j} \left(J\vec{S}_j + \vec{S}_j \times \vec{D}_{ij}\right) + \vec{H} \right] \cdot \vec{S}_i = \tag{1.21}$$

$$= -\sum_i \vec{H}_{\text{eff},i} \cdot \vec{S}_i$$

where $\sum_{i<j}$ iterates over the nearest neighbours of spin $\vec{S}_i$. The DMI term was modified via vector identity $\vec{D}_{ij} \cdot (\vec{S}_i \times \vec{S}_j) = \vec{S}_i \cdot (\vec{S}_j \times \vec{D}_{ij})$. The effective external field $\vec{H}_{\text{eff},i}$ depends on nearest neighbours of $\vec{S}_i$, but not on $\vec{S}_i$ itself ($\frac{\partial \vec{H}_{\text{eff}_i}}{\partial \vec{S}_i} = 0$). The same result is obtained if we calculate the field as a partial derivative of the Hamiltonian with respect to spin $\vec{S}_i$: $\vec{H}_{\text{eff},i} = \frac{\partial \mathcal{H}}{\partial \vec{S}_i}$.

$\vec{S}_i$ can be expressed in polar coordinates as θ_i, ϕ_i, where $\theta_i = 0°$ corresponds to the direction of the effective field. The Hamiltonian can be rewritten as

$$\mathcal{H} = -\sum_i \vec{H}_{\text{eff},i} \cdot \vec{S}_i = -\sum_i |\vec{H}_{\text{eff},i}| \cos\theta_i \tag{1.22}$$

The probability of finding $\vec{S}_i$ in solid angle $\mathrm{d}\omega_i = \sin\theta_i \mathrm{d}\theta_i \mathrm{d}\phi_i$ follows Maxwell-Boltzmann statistics

$$P(\theta_i, \phi_i) \sin\theta_i \mathrm{d}\theta_i \mathrm{d}\phi_i = C \exp\left(\frac{-|\vec{H}_{\mathrm{eff},i}| \cos\theta_i}{k_B T}\right) \sin\theta_i \mathrm{d}\theta_i \mathrm{d}\phi_i$$

$$1/C = \int_0^{2\pi} \mathrm{d}\phi \int_0^{\pi} \sin\theta_i \mathrm{d}\theta_i \exp\left(\frac{-|\vec{H}_{\mathrm{eff},i}| \cos\theta_i}{k_B T}\right) \tag{1.23}$$

Now we introduce variables R_i, R_i' sampled from uniform probability distribution $(0,1)$. The relationship between R_i and θ_i is defined by $P(\theta_i, \phi_i)$

$$R_i = \int_0^{2\pi} \mathrm{d}\phi_i \int_0^{\pi} \sin\theta_i \mathrm{d}\theta_i \mathrm{d}\phi_i$$

$$R_i' = \phi_i \, 2\pi \tag{1.24}$$

Energy does not depend on ϕ_i, so it follows uniform probability distribution $(0, 2\pi)$. To sample θ_i from distribution $P(\theta_i, \phi_i)$ using R from the uniform distribution, we need inverse of the equation above

$$\cos(\theta_i) = \frac{k_B T}{|\vec{H}_{\mathrm{eff},i}|} \log\left[\exp\left(\frac{|\vec{H}_{\mathrm{eff},i}|}{k_B T}\right)(1 - R_i) + R_i \exp\left(-\frac{|\vec{H}_{\mathrm{eff},i}|}{k_B T}\right)\right] \tag{1.25}$$

Assuming we run the heat bath algorithm on $L \times L$ lattice, the computational scheme is:

1. site $i \in 1, 2, ..., L^2$ is randomly selected

2. $\vec{H}_{\mathrm{eff},i}$ is calculated

3. random numbers R_i and R_i' are sampled from uniform distribution and θ_i, ϕ_i are calculated

4. θ_i, ϕ_i are transformed to original Cartesian coordinates into vector $\vec{S}_{\mathrm{new}}$

5. spin at site i is updated $\vec{S}_i \to \vec{S}_{\mathrm{new}}$

The main advantage of the heat bath compared to the Metropolis-Hastings algorithm is that all updates are automatically accepted and we do not need to tune the acceptance rate, resulting in faster convergence.

Simulated annealing

Simulated annealing is a technique used in optimization when searching for global minimum, for example via the Monte Carlo method. It is especially useful when the optimization problem contains lots of local minima. Some optimization algorithms can get stuck in a local minimum and cannot go over a barrier in the target function. Simulated annealing overcomes this problem by potentially accepting a worse proposed state with a certain probability based on the current "temperature", where the term "temperature" is abstract and does not necessarily mean the physical quantity. Metropolis-Hastings and Heat Bath algorithms already incorporate the idea of temperature, primarily to calculate finite-temperature simulations. However, this physical temperature is also used in the simulated annealing scheme to improve the search for the ground state.

Specifically in the classical Heisenberg model, the simulated annealing scheme is:

1. start with $T_0 > T_c$, where T_c is the ordering temperature

2. run Monte Carlo updates until the system is in thermal equilibrium (its total energy does not decrease anymore)

3. lower the temperature: $T_{i+1} < T_i$

4. repeat from step number 2 until $T_i \leq T_f$, where T_f is the final desired temperature (sufficiently close to 0 when searching for ground state)

1.6   Spin dynamics method

The spin dynamics method takes advantage of the Landau-Lifshitz-Gilbert (originally Landau-Lifshitz) equation (Landau and Lifshitz [1992]), which describes the evolution of the direction of a magnetic dipole moment in an external magnetic field.

Let us present a brief derivation of the equation inspired by Lakshmanan [2011]. We will begin with the Hamiltonian term for the interaction of the spin angular momentum operator with the external magnetic field:

$$\vec{S} = (S^x, S^y, S^z) \quad , \quad |\vec{S}| = 1$$
$$\mathcal{H}_H = -\frac{g\mu_B}{\hbar}\vec{S} \cdot \vec{B} \quad , \quad \vec{B} = \mu_0 \vec{H} \tag{1.26}$$

where g is the gyromagnetic ratio, μ_B is the Bohr magneton and μ_0 is permeability in vacuum. From the Schrödinger equation and Hellmann-Feynman theorem, we can write a dynamical equation for the spin expectation value

$$\frac{\mathrm{d}}{\mathrm{d}t}\langle\vec{S}(t)\rangle = \frac{g\mu_B}{\hbar}\langle\vec{S}(t) \times \vec{B}(t)\rangle \tag{1.27}$$

which leads to the Landau-Lifshitz equation for spin angular momentum without the damping term:

$$\frac{\mathrm{d}\vec{S}}{\mathrm{d}t} = -\gamma_0(\vec{S} \times \vec{H}) \tag{1.28}$$

This equation expresses the spin precession around the axis of the external field. However, it does not account for the spin relaxation process observed experimentally. Gilbert suggested adding a damping term, acting perpendicularly to the precession term, and ultimately aligning the spin collinearly to the external field.

$$\frac{\mathrm{d}\vec{S}}{\mathrm{d}t} = -\gamma_0\left[\vec{S} \times \vec{H}\right] + \alpha\gamma_0\left[\vec{S} \times \frac{\mathrm{d}\vec{S}}{\mathrm{d}t}\right] \tag{1.29}$$

where $\alpha \ll 1$ is the damping parameter which varies for different materials and is generally difficult to obtain (both experimentally and theoretically) (Nishino et al. [2020]). This equation can be rewritten as

$$(1 + \alpha^2\gamma_0)\frac{\mathrm{d}\vec{S}}{\mathrm{d}t} = -\gamma_0\left[\vec{S} \times \vec{H}\right] - \alpha\gamma_0\vec{S} \times \left[\vec{S} \times \vec{H}\right] \tag{1.30}$$

and further simplified by rescaling $\gamma = \gamma_0/(1 + \alpha^2\gamma_0)$

$$\frac{\mathrm{d}\vec{S}}{\mathrm{d}t} = -\gamma\vec{S} \times \vec{H} - \gamma\alpha\vec{S} \times \left[\vec{S} \times \vec{H}\right] \tag{1.31}$$
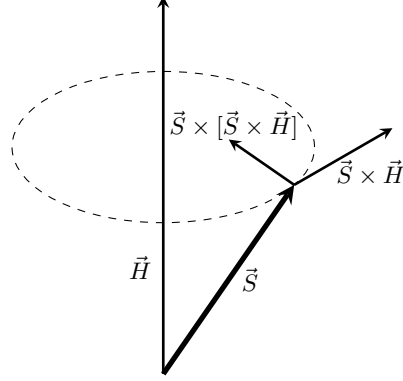

Figure 1.2: Spin precession around external field axis with damping.

To include the exchange interactions, we replace the magnetic field with arbitrary effective magnetic field $\vec{H}_{\mathrm{eff}}$, which can be expressed from the complete Hamiltonian, same as in Equation 1.21

$$\begin{aligned}
\mathcal{H} &= -J \sum_{<ij>} \vec{S}_i\vec{S}_j - \sum_{<ij>} \vec{D}_{ij} \cdot (\vec{S}_i \times \vec{S}_j) - \vec{H} \sum_i \vec{S}_i = \\
&= -\sum_i \vec{H}_{\mathrm{eff},i} \cdot \vec{S}_i
\end{aligned} \tag{1.32}$$

To conduct finite-temperature simulations, we need to extend the effective external field with the term for stochastic external field representing random thermal fluctuations (Skubic et al. [2008], Leliaert et al. [2017]):

$$\begin{aligned}
\vec{H}'_{\mathrm{eff},i} &= \vec{H}_{\mathrm{eff},i} + \vec{H}_{\mathrm{therm},i} \\
\vec{H}_{\mathrm{therm},i} &= \vec{\eta}\sqrt{\frac{2k_b T\alpha}{\gamma}}
\end{aligned} \tag{1.33}$$

where $\vec{\eta}$ is a random vector drawn from the standard normal distribution, such that:

$$\begin{aligned}
\langle\vec{H}_{\mathrm{therm},i}(t)\rangle &= 0 \\
\langle\vec{H}_{\mathrm{therm},i}(t_1)\vec{H}_{\mathrm{therm},j}(t_2)\rangle &= \frac{2k_b T\alpha}{\gamma}\delta_{ij}\delta(t_1 - t_2)
\end{aligned} \tag{1.34}$$

meaning that the field is not correlated across different spin sites and time.

1.7 Motivation - materials of interest

The thesis focuses on investigating the effect of DMI on triangular two-dimensional spin lattices (described in section 2.2).

The theoretical results are potentially comparable to experimental results, as there are known compounds matching the following description:

- magnetic atoms are arranged in planes with triangular planar symmetry

- individual planes are separated by sufficient distance so that inter-planar interactions can be neglected

- inversion symmetry is broken (non-centrosymmetric), usually by additional non-magnetic atoms

One example of such compound is $EuAl_{12}O_{19}$, where magnetic Eu ions are arranged in planar triangular lattices. The exchange interaction between the europium ions is mediated by the oxygen atoms (superexchange). The Eu-O-Eu bond forms an angle of $175.5° \neq 180°$ [1] (Jain et al. [2013]) – the inversion symmetry is broken and DMI is allowed. In this case, the DMI vector points in the out-of-plane direction.

Another such compound is $Ba_3CoSb_2O_9$ (Fortune et al. [2021]). Other samples matching the theoretical description are layered samples, such as ultrathin magnetic films.

---

[1]Data retrieved from the Materials Project for EuAl12O19 (mp-1212749) from database version v2022.10.28.

2. Methods

2.1 UppASD and pyUppASD

All numerical results in this thesis have been computed using UppASD. The UppASD (Uppsala Atomistic Spin Dynamics) package is a simulation tool for atomistic spin dynamics at finite temperatures (Skubic et al. [2008]). It implements all methods described in section 1.5: Metropolis and heat bath algorithms for the Markov Chain Monte Carlo method and the spin dynamics method using the Landau–Lifshitz–Gilbert equation. It can leverage multi-core processors and vectorization for efficiency.

To run a simulation, a set of text-based configuration files needs to be defined first. This includes the lattice, inter-atomic interactions, external field, temperature, initial state, computation method, observable sampling, and more.

UppASD can then be launched, producing text-based output files with measurements and resulting lattice.

To conduct more complicated experiments, like the heat capacity measurement (subsection 3.2.1) or hysteresis loop measurement section 3.3, users need to implement a considerable portion of the logic themselves (e.g. in Bash) and chain individual UppASD executions together.

To simplify this, we introduce *pyUppASD*, a wrapper library for UppASD written in Python, which has been developed as a part of this thesis. It allows users to define complicated experiments programmatically in Python and access the simulation results in the form of Numpy (Harris et al. [2020]) arrays. It also features some basic capabilities of plotting or animating resulting lattices. It is distributed as open-source software and available at `https://github.com/janpriessnitz/pyUppASD`.
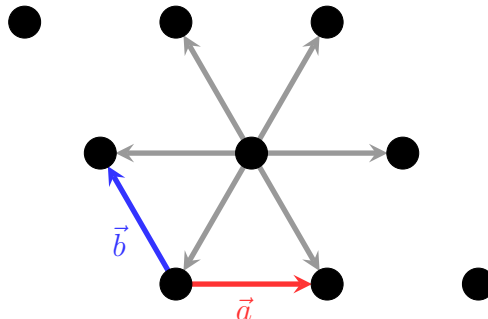
2.2 Studied system

2.2.1 Lattice

Figure 2.1: 2D triangular lattice studied in this thesis. The red and blue arrows show the basis vectors of the lattice. Grey arrows point to the 6 nearest neighbours of the central site.

The studied system is based on a two-dimensional triangular lattice. The unit cell of the lattice contains a single site with a magnetic moment. In this experiment, we place the magnetic site at the origin (coordinates $(0,0)$), although the site placement is irrelevant in this case (a single site per unit cell). Multiple valid choices for unit cell dimensions are available. Here, we generate the lattice using two basis vectors: $\vec{a} = (1,0)$ and $\vec{b} = (-1/2, \sqrt{3}/2)$.

Each site has got six equivalent nearest neighbours, with unit distance from the site. The translation vectors to the nearest neighbours expressed both in the real coordinate system and the coordinate system of the basis vectors, are:

- $\vec{n}_1 = (1,0) = 1\vec{a} + 0\vec{b}$

- $\vec{n}_2 = (1/2, \sqrt{3}/2) = 1\vec{a} + 1\vec{b}$

- $\vec{n}_3 = (-1/2, \sqrt{3}/2) = 0\vec{a} + 1\vec{b}$

- $\vec{n}_4 = (-1,0) = -1\vec{a} + 0\vec{b}$

- $\vec{n}_5 = (-1/2, -\sqrt{3}/2) = -1\vec{a} - 1\vec{b}$

- $\vec{n}_6 = (1/2, -\sqrt{3}/2) = 0\vec{a} - 1\vec{b}$

The boundary conditions of the lattice are chosen to be periodic, meaning that the lattice sites are bound by the condition:

$$\vec{S}(N + k, M + l) = \vec{S}(k, l) \tag{2.1}$$

where $\vec{S}(k,l)$ is the spin of the magnetic dipole located at $k\vec{a} + l\vec{b}$ and N and M are the lattice dimensions in respective directions. In this thesis, we choose N and M divisible by 3, since the observed antiferromagnetic phases have a propagation vector of $(1/3, 1/3)$.

We use the Heisenberg model, meaning that each magnetic moment is represented by a 3-dimensional vector of constant magnitude. Bohr magneton (μ_{B}) is selected as the primary unit of magnetic dipole moment in this simulation. Each lattice site has got a magnetic dipole with a moment of 1 μ_{B}.

2.2.2 Hamiltonian

In the studied system, we consider 3 types of interactions:

- exchange interaction J

- Dzyaloshinskii-Moriya interaction D
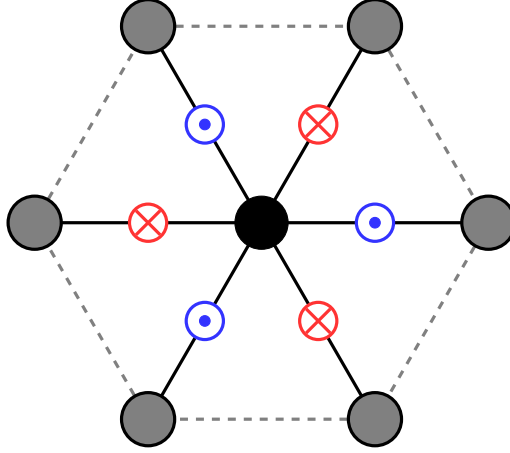
- interaction with external field H

Figure 2.2: Scheme of nearest neighbours in the studied system. Solid black lines indicate the interaction between the central site and its neighbours. Smaller red and blue circles indicate the directions of the respective DMI vectors. Red means into the paper, blue means out of the paper.

The exchange and DM interaction are considered only between nearest neighbours. All interactions between more distant sites are neglected. The Hamiltonian can be expressed as:

$$\mathcal{H} = -J \sum_{<ij>} \vec{S}_i \cdot \vec{S}_j - \sum_{<ij>} \vec{D}_{ij} \cdot (\vec{S}_i \times \vec{S}_j) - \vec{H} \cdot \left(\sum_i \vec{S}_i \right) \qquad (2.2)$$

where $< ij >$ iterates over all pairs of nearest neighbours. The DMI vector $\vec{D}_{ij}$ depends on the relative position of i-th and j-th moment denoted as $\vec{u}_{ij}$:

$$\vec{D}_{ij} = \begin{cases} (0, 0, D) & \text{if } \vec{u}_{ij} \in \{(1/2, \sqrt{3}/2), (-1, 0), (1/2, -\sqrt{3}/2)\} \\ (0, 0, -D) & \text{if } \vec{u}_{ij} \in \{(1, 0), (-1/2, \sqrt{3}/2), (-1/2, -\sqrt{3}/2)\} \end{cases} \qquad (2.3)$$

The strength of the interactions is specified by $J, D, H \in \mathbb{R}$. These are the most influential parameters of the simulation, governing the behaviour of the simulated systems. Since we are not interested in the total energy scale, we set $J \pm 1$ and specify D and H in units of $|J|$. This contracts the parameter space.

From the definition of $\vec{D}_{ij}$, we see that the DMI vector points of out the lattice plane. In-plane DMI is the subject of extensive study yielding different results (Hog et al. [2022], Aldarawsheh et al. [2023]), but is out of the scope of this thesis.

2.3 Method

In chapter 1, we discussed the principles of computational methods used in this thesis. In this section, we will focus on the practical aspects of the individual simulation experiments. They will include, among others:

- computational schemes (algorithms)

- parameters of the simulations

- available observables and their sampling

2.3.1 Ground state

Finding the ground state of the studied lattice is an important simulation that shows us fundamental information about the lattice.

We start with a random lattice of $L \times L$ sites ($L = 90$, $L = 180$, or $L = 270$ in this thesis): the moment vector at each site is individually set to a random direction. From this state, we begin the process of simulated annealing. We start with an initial temperature T_0 and end with a final temperature T_f. The process is divided into N temperature steps with temperatures $T_0, T_1, ..., T_{N-1} = T_f$. In each temperature step, we make M Markov Chain update sweeps across the lattice, meaning $M \cdot L \cdot L$ individual updates. The simulated annealing temperature schedule (values of T_i) is chosen so that the temperatures follow the geometric sequence:

$$T_i = T_0 \cdot a^i \quad , \quad a = (\frac{T_f}{T_0})^{\frac{1}{N}} \tag{2.4}$$

We also need to choose the Markov Chain update algorithm. UppASD offers Metropolis or heat bath update algorithms (described in section 1.5). We compare the two on a limited set of parameters to ensure that they are consistent and give equivalent results. Further on, we use the heat bath algorithm, because the lattice reaches equilibrium faster (using less update steps and computation time).

To obtain a good result (a state close to the true ground state), we need to fulfill two important conditions:

- The starting temperature must be sufficiently high so that when the lattice reaches equilibrium at this temperature, it is still random. In particular, the starting temperature must be above the critical ordering temperature of the system.

- The number of steps N and M must be large enough so that a) equilibrium is achieved at the end of each temperature step, and b) the temperature drop between two temperature steps is not too big. This ensures that the annealing process is approximately adiabatic (quasi-static).

We found that $T_0 = 1000$ K, $T_f = 0.01$ K, $N = 30$ is a satisfactory temperature scale for our system. M in range of $10000 \leq M \leq 100000$ is sufficient depending on specific conditions like J, D and H. Ideally, we would need $T_f = 0$ K to observe the true ground state. Zero temperature is principally impossible to reach with simulated annealing. Instead, we require $\lim(T_f) = 0$. $T_f = 0.01$ K is small enough for the purposes of this thesis.

The initial simulated annealing phase is followed by the measurement phase with fixed temperature T_f. The measurement phase is useful when measuring observables at finite temperatures. Here, the ground state is found at the end of the initial annealing phase and the measurement phase can be skipped.

2.3.2 Observables

We can calculate several characteristic observables of the ground state to better understand it. Most importantly, it helps us with classifying the magnetic ordering.

In this thesis, we will present the following observables when investigating ground states:

- magnetization $\vec{M} = \frac{1}{L^2} \sum_i \vec{S}_i$

- static spin structure factor $\tilde{S}(\vec{k})$

- magnetic susceptibility tensor $\xi_{\alpha\beta} = M_\alpha / H_\beta$

- total energy and Hamiltonian projections with respect to individual interaction types E_{tot}, E_J, E_D, E_H

Static spin structure factor is a useful quantity that clearly shows spatial periodicity in the lattice. It is very similar to the conventional structure factor widely used in crystallography:

$$\begin{aligned}
\tilde{S}(\vec{k}) &= \frac{1}{L^2} \sum_i \sum_j (\vec{S}_i \cdot \vec{S}_j) e^{i\vec{k}\cdot(\vec{r}_i - \vec{r}_j)} \\
&= \frac{1}{L^2} (\sum_i \vec{S}_i e^{i\vec{k}\cdot\vec{r}_i})(\sum_j \vec{S}_j e^{-i\vec{k}\cdot\vec{r}_j})
\end{aligned} \tag{2.5}$$

To reduce noise, multiple independent lattices (ensembles) are simulated and the measured observables are averaged.

2.3.3 Finite-temperature measurements

In the section above, we described how to obtain zero-temperature properties of a lattice. We might also be interested in those same properties but at finite temperatures. The method for measuring finite-temperature properties is very similar. The first step is simulated annealing, only with T_f not approaching 0, but the temperature of interest.

However, the measurement phase itself is principally different: at finite temperatures, there is no single ground state available. Instead, there is a thermodynamic ensemble of possible states at a certain energy. To correctly measure any observable, we need to calculate the thermodynamic average of such observable by sampling over the thermodynamic ensemble. Assuming the system is in equilibrium, this is achieved by applying Markov Chain updates upon the lattice and periodically sampling the observables.

2.3.4 Heat capacity

Heat capacity is measured to find the critical ordering temperature of the lattice. First, the ground state is found using the method described above. Then, we run a temperature sweep: N temperature steps with increasing temperatures $T_{i+1} > T_i$. In each step, the lattice first reaches the equilibrium. After that, the observables are sampled in the same way as was described in subsection 2.3.3. Here, we measure energy, magnetization and its higher moments. Temperature-averaged variables are enclosed in $\langle ... \rangle$.

The specific heat capacity is calculated from measured energy:

$$c_V = \frac{1}{L^2} \frac{\mathrm{d}\langle E \rangle}{\mathrm{d}T} \tag{2.6}$$

Binder cumulant can be used to precisely determine the critical ordering temperature (Landau and Binder [2009]). It can eliminate the inaccuracy which originates from the finite size of the simulated system:

$$U_L = 1 - \frac{\langle M^4 \rangle}{\langle M^2 \rangle^2} \tag{2.7}$$

To determine the critical temperature, the Binder cumulant versus temperature dependency needs to be measured for multiple lattice sizes.

2.3.5 Hysteresis loop

The hysteresis loop is measured as a sweep over all values of an external field. Let us first define the saturation external field H_S as the minimal external field strength needed to achieve maximal magnetization ($|M| = 1$ in our case).

We start with a lattice that is fully saturated. This is achieved by performing simulated annealing down to the desired temperature with initial external field $|\vec{H_{max}}| > |\vec{H_S}|$.

The next phase employs the spin dynamics algorithm, Markov Chain Monte Carlo is not used anymore. It consists of $2N$ steps, during which we sweep through the external field strength range. In each step, we first update the external field $H_i \to H_{i+1}$. After that, M spin dynamics timesteps are carried out. Again, M must be large enough so that the lattice can reach equilibrium and the process can be considered quasi-static. Finally, magnetization is measured and the external field is updated again.

A simple sweep is a linear sequence from negative to positive values and back:

$$
\begin{aligned}
H_0 &= -H_{max} \\
H_i &= H_{max}(-1 + \frac{2i}{N}) \quad, \quad \text{if } 0 < \text{i} < \text{N} \\
H_{N-1} &= H_{max} \\
H_{N+i} &= H_{max}(1 - \frac{2i}{N}) \quad, \quad \text{if } \text{N} < \text{i} < \text{2N}
\end{aligned}
\tag{2.8}
$$

which corresponds to N steps from $-H_{max}$ to H_{max} and N steps from H_{max} to $-H_{max}$.

This sequence can be improved by "slowing down" at critical points:

1. $N_1/2$ steps from $-H_{max}$ to $-H_{thresh}$

2. N_2 steps from $-H_{thresh}$ to H_{thresh}

3. $N_1/2$ steps from H_{thresh} to H_{max}

and analogically from H_{max} to $-H_{max}$. Note that $0 \leq H_{thresh} \leq H_{max}$.

Hysteresis loop can be measured for various values of J and D, but also temperature T (subsection 3.3.2).

All spin dynamics simulations in this thesis use timestep $\Delta t = 10^{-15}$ s and damping parameter $\alpha = 0.05$.

3. Results

3.1 Ground state (zero-temperature)

In this section, we will present the ground states (lowest-energy states) of the studied lattice at zero temperature for various parameter settings - we will explore the parameter space of the Hamiltonian defined in the previous chapter (subsection 2.2.2). We used heat bath MCMC with the simulated annealing technique to calculate the ground states. The method is described in detail in section 1.5.

3.1.1 Qualitative analysis

To get a basic overview of all possible orderings of the lattice, we first show small-scale lattices for a few selected parameter sets without the external magnetic field ($\vec{H} = (0, 0, 0)$). The following figures illustrate 30×30 lattice states in the form of x, y, and z components of the magnetic moment vectors.

Ferromagnetic exchange interaction
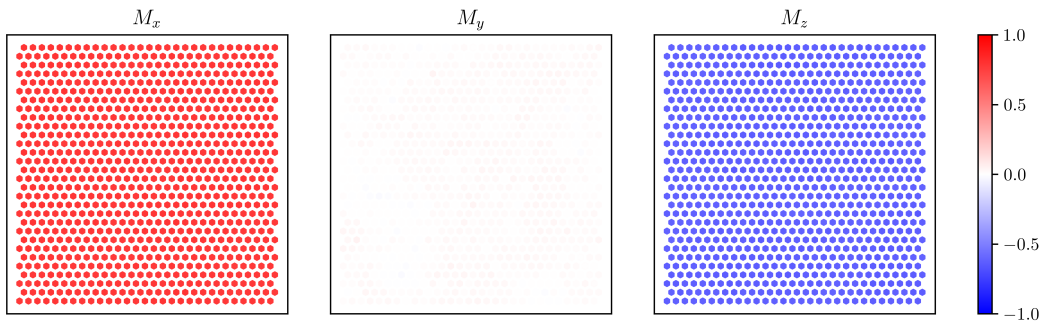
Figure 3.1: Ground state lattice for $J = 1$, $D = 0$.

We start without the DMI ($D = 0$), only with exchange interaction $J = 1$ which favours parallel orientation of neighbouring spins. The resulting state is shown in Figure 3.1 is a ferromagnetic ordering in an arbitrary direction, i. e. it is not particularly oriented with respect to the lattice plane.
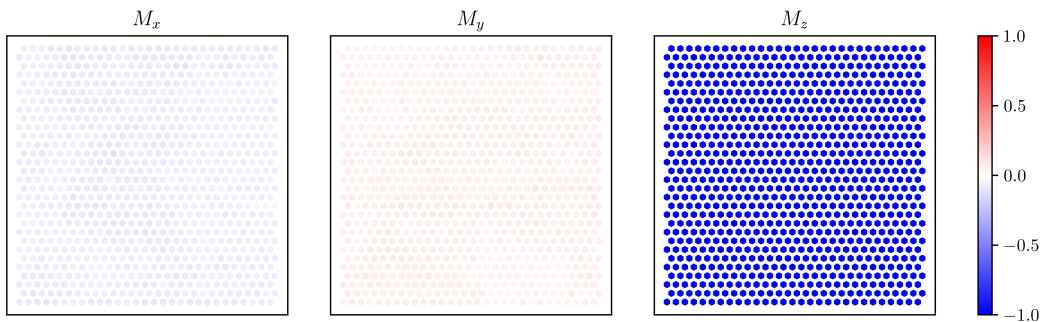
Figure 3.2: Ground state lattice for $J = 1$, $D = 1$.

In the next step, we enable the DMI. Figure 3.2 shows ground state for $J = 1$, $D = 1$ which is ferromagnetic as well. However, we can notice that the magnetic moments are oriented in the z-direction, perpendicular to the lattice plane. This is an effect of the DMI and it is more closely investigated in subsection 3.2.3.
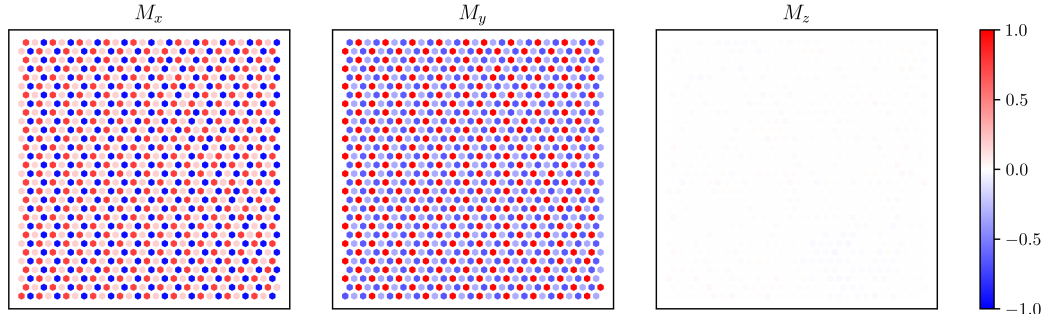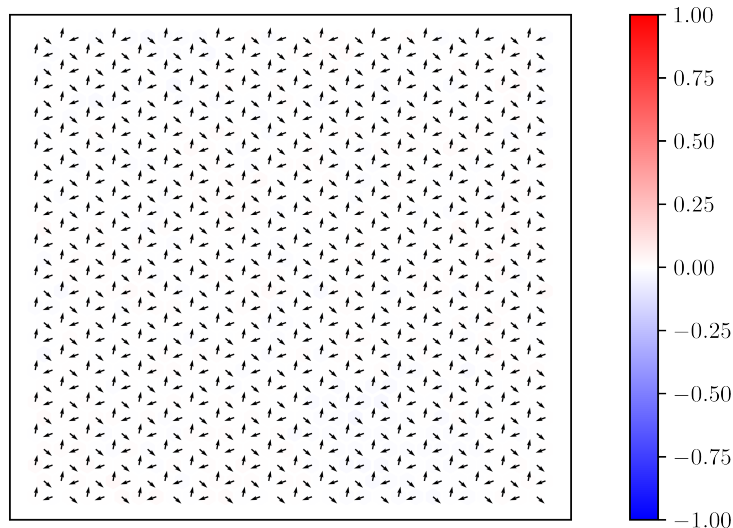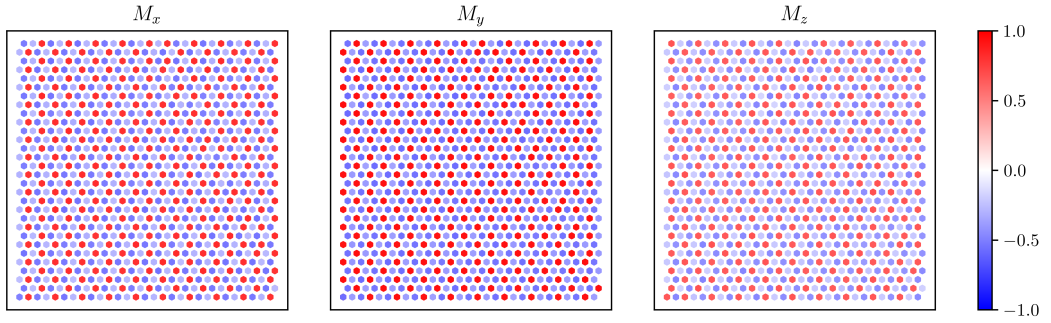

Figure 3.3: Ground state lattice for $J = 1$, $D = 1.8$.

Figure 3.4: Ground state lattice for $J = 1$, $D = 1.8$. Alternative plot showing the in-plane cycloidal ordering. Arrows show in-plane spin component, white background colour means zero z-component.

The DMI can be further strengthened, which results in a sharp phase transition. Figure 3.3 and Figure 3.4 shows ground state for $J = 1$ and $D = 1.8$. The order is antiferromagnetic, cycloidal with propagation vector $\vec{k} = (1/3, 1/3)$, meaning that neighbouring magnetic moments form an angle of 120°. Note that the moments rotate inside the lattice plane, the rotation axis lies in the z-direction. Identical antiferromagnetic ordering was observed in Hog et al. [2022].

Antiferromagnetic exchange interaction

Figure 3.5: Ground state lattice for $J = -1$, $D = 0$.
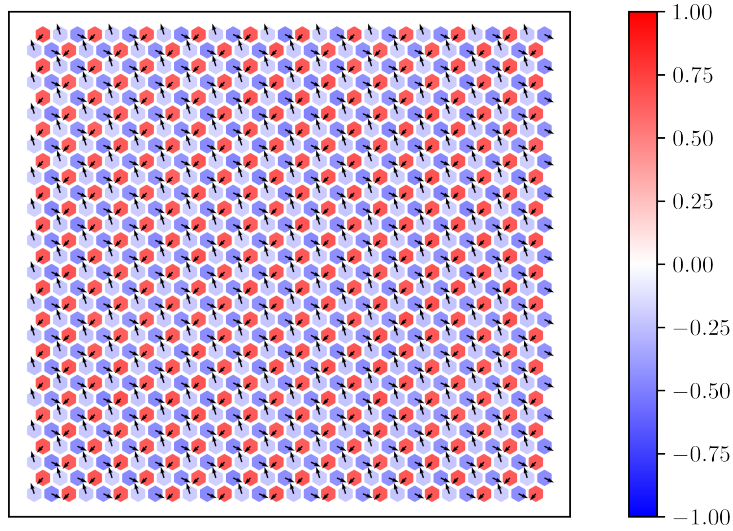
Figure 3.6: Ground state lattice for $J = -1$, $D = 0$. Alternative plot showing the cycloidal ordering. Arrows show in-plane spin component, colour shows z-component.

Figure 3.5 and Figure 3.6 shows the ground state with no DMI and antiferromagnetic exchange interaction ($J = -1$, $D = 0$). The order is antiferromagnetic, cycloidal with propagation vector $\vec{k} = (1/3, 1/3)$. The plane of rotation of the magnetic moment is arbitrary – z-component of spins is non-zero.
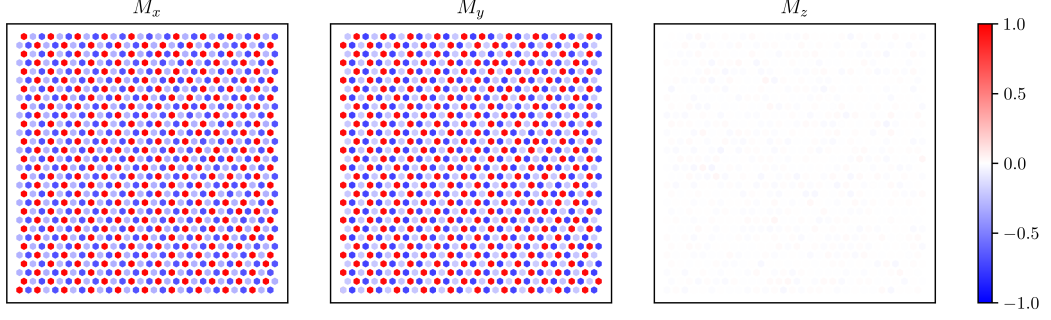
Figure 3.7: Ground state lattice for $J = -1$, $D = 0.1$.

Next, we include small DMI: $D = 0.1$. In Figure 3.7 of the ground state, we see that the antiferromagnetic order has not changed, but it is now oriented such that the moments rotate inside the lattice plane, the same way as in the case $J = 1$, $D = 1.8$. This was also observed in Hog et al. [2022].

Antiferromagnetic exchange interaction $J = -1$ is not covered further, because quantum effects, neglected by the classical Heisenberg model, play a significant role there (as explained in the theoretical part).

Spin structure factor
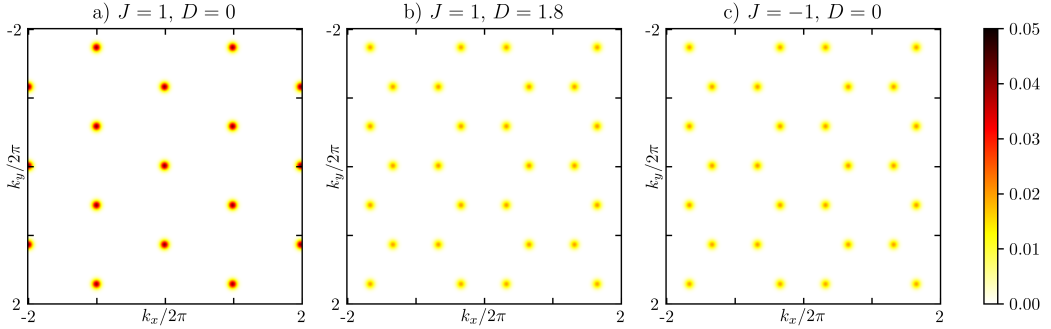
Figure 3.8: Spin structure factor of various ground states: a) ferromagnetic order, b) antiferromagnetic order caused by strong DMI, c) antiferromagnetic order caused by antiferromagnetic exchange interaction.

Figure 3.8 shows the spin structure factor of ground states shown in the section above. Hexagonal symmetry is clearly visible in all three plots – the magnetic order does not decrease the symmetry of the underlying lattice. The scale of the k-vector is defined by the inter-site distance of the lattice, which was set to 1.
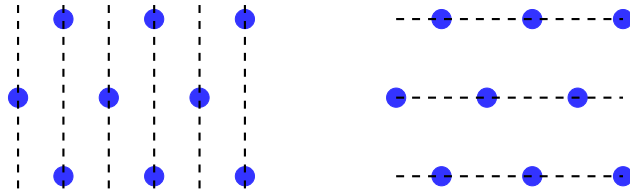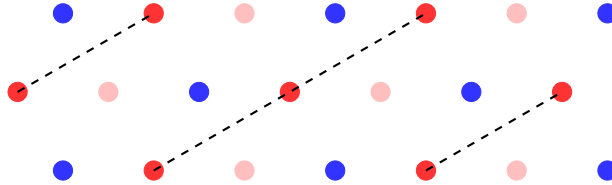

Figure 3.9: Crystallographic planes in the ferromagnetic lattice belonging to the spin structure factor peaks at $\vec{k} = (0, \pm\frac{4\pi}{\sqrt{3}})$.

In the ferromagnetic lattice, there are 3 sets of equivalent spin structure factor peaks. Peak at $\vec{k} = (0,0)$ implies non-zero overall magnetization, peaks at $|\vec{k}| = \frac{4\pi}{\sqrt{3}}$ correspond to the inter-planar distance $d = \frac{\sqrt{3}}{2}$, peaks at $|\vec{k}| = 4\pi$ correspond to distance $d = \frac{1}{2}$.

In the antiferromagnetic lattice, the central peak at $\vec{k} = (0,0)$ is missing as expected. The first set of peaks is located at $|\vec{k}| = \frac{4\pi}{3}$. Figure 3.1.1 shows the crystallographic plane family belonging to these peaks.

Figure 3.10: Crystallographic planes in the antiferromagnetic lattice belonging to the spin structure factor peaks at $\vec{k} = \pm\frac{4\pi}{3}(\frac{1}{2}, \frac{\sqrt{3}}{2})$. Interplanar distance is $d = \frac{3}{2}$.

We can use the k-vectors to write an equation for the spin vectors in this in-plane antiferromagnetic order. A spin vector located at $\vec{r} = (r_x, r_y)$ is:

$$\vec{S}(\vec{r}) = (\mathrm{Re}[e^{i\vec{k}\vec{r}}], \mathrm{Im}[e^{i\vec{k}\vec{r}}], 0) \tag{3.1}$$

where the origin of the $\vec{r}$ coordinate system can be freely chosen to accommodate for the phase shift.

Using the spin structure factor to identify phases in the lattice has significant advantages compared to using other quantities, such as magnetization. The spin structure factor is unique for the specific phase so that equal spin structure factor implicates equal phase and vice versa. Such a claim does not hold for magnetization. This also means that it can be averaged over many simulation ensembles to reduce noise. Spin structure factor is used in section 3.4.

3.1.2 Phase diagrams

In the last section, we have seen possible magnetic orders in the lattice. Now is the time to examine the Hamiltonian parameter space in more detail and find the ground state for each possible combination of parameters. Exchange interaction is set to $J = 1$ since there is no need to explore other values (as explained in subsection 2.2.2). Other parameters are a) strength of DMI (or D), and b) either in-plane or out-of-plane component of the external field vector (H_x or H_z). The results are plotted in the form of a phase diagram showing the magnetization of the lattice state.

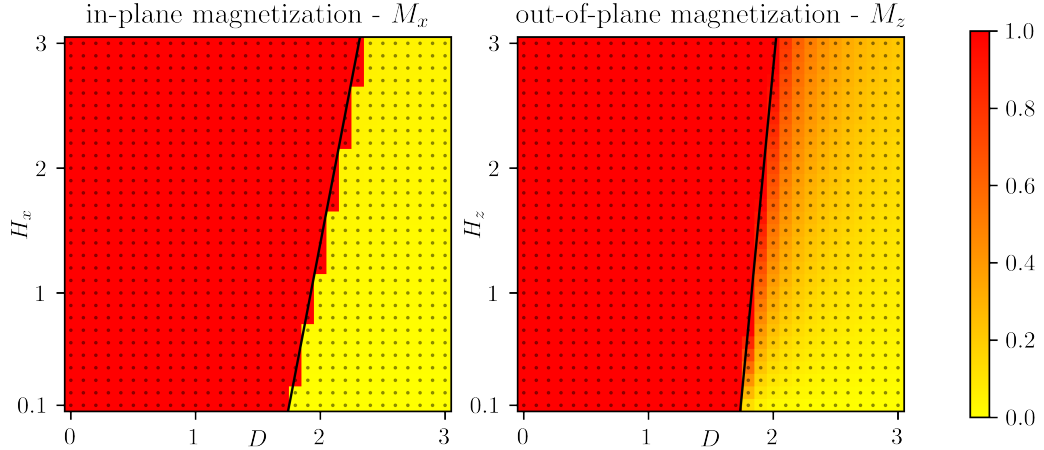Figure 3.11: Phase diagram featuring magnetization with ferromagnetic exchange interaction ($J = 1$). The external field is either in-plane (left) or out-of-plane (right). Red colour ($M = 1$) corresponds to ferromagnetic order. Yellow colour ($M = 0$) means antiferromagnetic order. Grey dots show individual measuring points. The black line shows the analytically calculated phase transition from subsection 3.1.3. $L = 90$.

When applying external magnetic field, new magnetic phases can be induced. These phases are usually called metamagnetic and the related magnetic phase transitions with respect to the external magnetic field as the control parameter are called metamagnetic transitions. A phase transition between two magnetic phases can be a first- or second-order type depending on whether it is connected with a discontinuity of the first derivative (e.g., magnetization) or the second derivative (e.g., magnetic susceptibility) of the magnetic part of the free energy (Sechovský [2001]).

In the in-plane case, the phase boundary is sharp (from completely ferromagnetic to completely antiferromagnetic). It can be classified as a first-order phase transition, because of the discontinuity of magnetization on the phase boundary. The transition can be observed, for example, using the spin dynamics method, finite temperature and varying external field: we start with parameters favouring the ferromagnetic order, find the ground state, then run spin dynamics while gradually decreasing the external field strength. This is essentially the experimental setup for measuring the hysteresis loop. Figure 3.12 shows a snapshot lattice from the measurement of hysteresis loop (from section 3.3) featuring first-order phase transition.
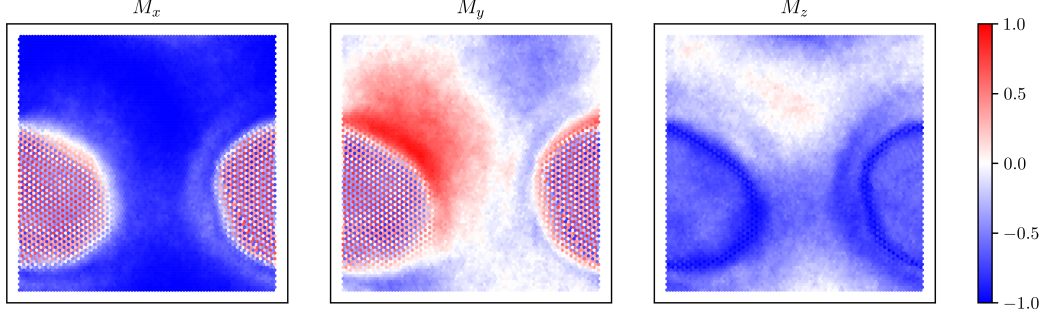
Figure 3.12: Intermediate lattice state featuring first-order phase transition from ferromagnetic to antiferromagnetic phase. Lattice obtained via spin dynamics method with $J = 1$, $D = 2$, $T = 0.013$, and varying in-plane external field.

In the out-of-plane case, the phase transition is gradual – for $D > \sqrt{3}$, magnetization M_z gradually increases with increasing external field H_z. The corresponding lattice state can be classified as conical. It is a mixture of the antiferromagnetic order with moments rotating in-plane and ferromagnetic order with non-zero z-component of the moment vectors. This state can be characterized via an equation for the spin vectors, similarly to Equation 3.1:

$$\vec{S}(\vec{r}) = (\sqrt{1 - S^{z2}}\ \mathrm{Re}[e^{i\vec{k}\vec{r}}], \sqrt{1 - S^{z2}}\ \mathrm{Im}[e^{i\vec{k}\vec{r}}], S^z) \tag{3.2}$$
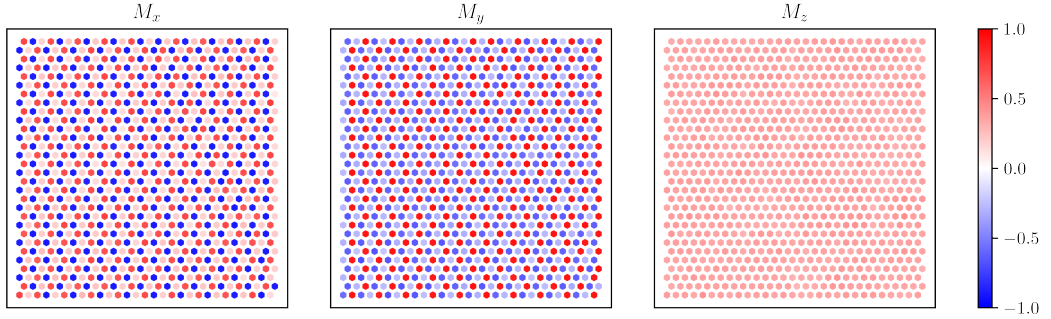
where $-1 \leq S^z \leq 1$ and $S^z = M_z$.

Figure 3.13: Lattice state with conical magnetic order for $J = 1$, $D = 2$, $H_z = 1$.

Let us investigate the out-of-plane magnetization seen in Figure 3.11 more closely, namely the region $D > \sqrt{3}$.
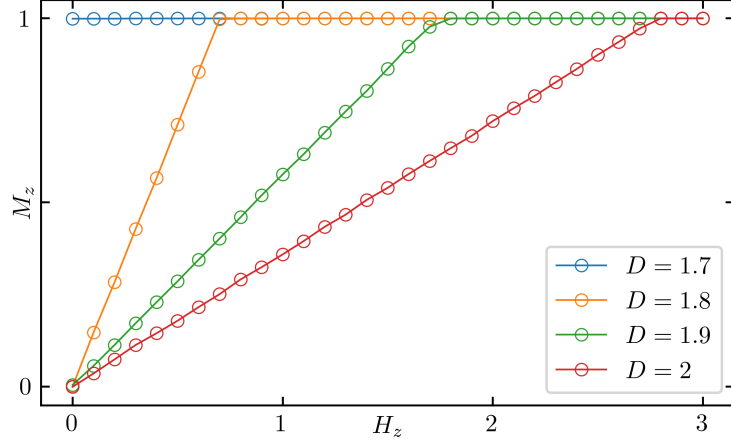
Figure 3.14: Measured out-of-plane magnetization M_z vs. external field H_z for $J = 1$ and various D.

Figure 3.14 shows that the dependence of M_z on H_z is linear up until saturation $M_z = 1$. This means that the magnetic susceptibility is constant throughout the external magnetic field range $(0, H_s)$ where H_s is the saturation external field: At H_s, susceptibility drops to zero, indicating second-order phase transition.

$$\chi = \frac{M}{H} = \frac{1}{H_s} \tag{3.3}$$

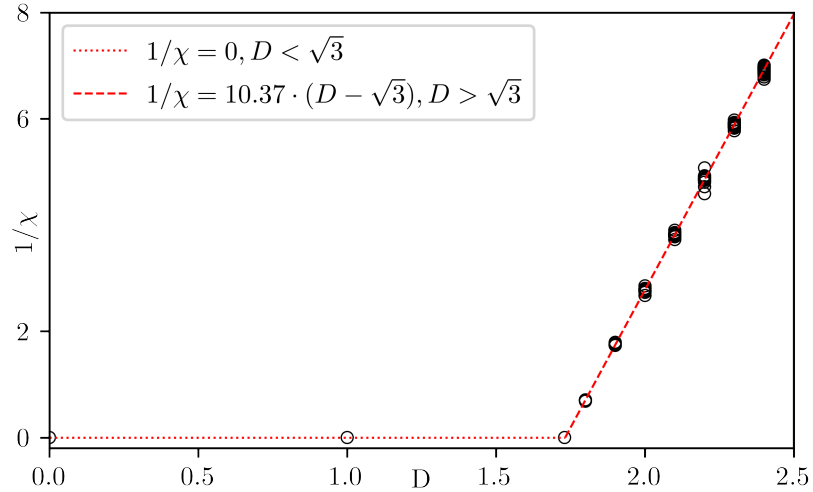Saturation external field and susceptibility are only dependent on DMI strength D.

Figure 3.15: Inverse of magnetic susceptibility vs. DMI strength D. $1/\chi = 0$ for $D < \sqrt{3}$ indicating ferromagnetic order. The red dashed line is a fit obtained via the least-squares method.

3.1.3   Analytical solution

Only two magnetic orderings are present in the phase diagrams presented above. We will assume that this is correct and no other phases can appear. This situa-

tion is simple enough so that the phase diagrams can be derived from analytical calculations. We will resolve the Hamiltonian for each phase and obtain its energy. We can compare these energies and determine which phase is favored for a set of Hamiltonian parameters. Let us first write down some useful relations:

$$E = E_J + E_D + E_H$$

$$E_H = -\vec{H} \sum_i \vec{S}_i = -L^2 \vec{H} \cdot \vec{M}$$

$$E_J = -J \sum_{<ij>} \vec{S}_i \cdot \vec{S}_J = -J \sum_{<ij>} |\vec{S}_i||\vec{S}_j| \cos \alpha_{ij} = -J \sum_{<ij>} \cos \alpha_{ij}$$

$$E_D = -D \sum_{<ij>} (0,0,\pm 1) \cdot (\vec{S}_i \times \vec{S}_j) =$$

$$= -D \sum_{<ij>} (0,0,\pm 1) \cdot (S_i^y S_j^z - S_i^z S_j^y; S_i^z S_j^x - S_i^x S_j^z; S_i^x S_j^y - S_i^y S_j^x) =$$

$$= -D \sum_{<ij>} \pm (S_i^x S_j^y - S_i^y S_j^x) = -D \sum_{<ij>} \pm S_i^\perp S_j^\perp \sin \alpha_{ij}^\perp$$

$$S^\perp = \sqrt{S^{x2} + S^{y2}}$$

(3.4)

where α_{ij} denotes the counterclockwise angle between the spin vectors $\vec{S}_i$ and $\vec{S}_j$, $\alpha_{ij}^\perp$ denotes the angle between the vectors' in-plane projections and the $\pm$ sign behaves such that the calculation is consistent with DMI vector defined in Equation 2.3.

Let us start by calculating the energy of the purely antiferromagnetic phase, defined using Equation 3.1 and $\vec{k} = (\frac{4\pi}{3}, 0)$. From the definition, it follows that α_{ij} only depends on $\vec{r}_i - \vec{r}_j$. The angle between a site and its nearest neighbour in a certain direction is therefore constant (the translation vectors are written down in subsection 2.2.1). Since $S^z = 0$, $\alpha_{ij} = \alpha_{ij}^\perp$.

$$\alpha_{ij} = \vec{k} \cdot (\vec{r}_i - \vec{r}_j)$$

$$\bar{\alpha}_1 = \vec{k} \cdot \vec{n_1} = (\frac{4\pi}{3}, 0) \cdot (1, 0) = \frac{4\pi}{3}$$

$$...$$

$$\bar{\alpha}_6 = \vec{k} \cdot \vec{n_6}$$

$$\bar{\alpha}_1 = \bar{\alpha}_3 = \bar{\alpha}_5 = \frac{4\pi}{3} = 240°$$

$$\bar{\alpha}_2 = \bar{\alpha}_4 = \bar{\alpha}_6 = \frac{2\pi}{3} = 120°$$

(3.5)

where $\bar{\alpha}_i$ denotes the angle between a site and its i-th nearest neighbour.

$$E_H^{AFM} = -L^2 \vec{H} \cdot \vec{M} = 0$$
$$E_J^{AFM} = -J \sum_{<ij>} \cos \alpha_{ij} = -J \sum_i (\cos \bar{\alpha}_1 + ... + \cos \bar{\alpha}_6) =$$
$$= -JL^2 (3 \cos \frac{2\pi}{3} + 3 \cos \frac{4\pi}{3}) = -JL^2 (-\frac{3}{2} - \frac{3}{2}) = 3JL^2$$
$$E_D^{AFM} = -D \sum_{<ij>} \pm S_i^\perp S_j^\perp \sin \alpha_{ij}^\perp = -D \sum_{<ij>} \pm \sin \alpha_{ij} = \qquad (3.6)$$
$$= -D \sum_i (-\sin \bar{\alpha}_1 + \sin \bar{\alpha}_2 - \sin \bar{\alpha}_3 + \sin \bar{\alpha}_4 - \sin \bar{\alpha}_5 + \sin \bar{\alpha}_6) =$$
$$= -DL^2 (3 \sin \frac{2\pi}{3} - 3 \sin \frac{4\pi}{3}) = -3\sqrt{3}DL^2$$
$$E^{AFM} = 3JL^2 - 3\sqrt{3}DL^2 = 3L^2 (J - \sqrt{3}D)$$

Now to the ferromagnetic order. We assume that $|\vec{M}| = 1$, $\vec{M} \parallel \vec{H}$ and $\alpha_{ij} = 0$:

$$E_H^{FM} = -L^2 \vec{H} \cdot \vec{M} = -L^2 |\vec{H}|$$
$$E_J^{FM} = -J \sum_{<ij>} \cos \alpha_{ij} = -6JL^2$$
$$E_D^{FM} = -D \sum_{<ij>} \pm S_i^\perp S_j^\perp \sin \alpha_{ij}^\perp = 0 \qquad (3.7)$$
$$E^{FM} = -L^2 |\vec{H}| - 6JL^2 = L^2 (-\vec{H} - 6J)$$

We can calculate the position of the phase boundary by comparing E^{AFM} and E^{FM}:

$$E^{AFM} = E^{FM}$$
$$3L^2 (J - \sqrt{3}D) = L^2 (-|\vec{H}| - 6J) \qquad (3.8)$$
$$-3\sqrt{3}D = -\vec{H} - 9J$$

for the $J = 1$ case:

$$-3\sqrt{3}D = -|\vec{H}| - 9$$
$$|\vec{H}| = 3\sqrt{3}D - 9 \qquad (3.9)$$

This phase boundary expression is consistent with the observed phase diagram in Figure 3.11.

The out-of-plane external field case needs to be calculated differently because there exists a mixed state between ferromagnetic and antiferromagnetic order (conical ordering) satisfying Equation 3.2. We will compute the energy of a single

mixed phase with variable S^z, then find S^z_{min} for which the energy is minimized:

$$|\vec{S}| = 1 = \sqrt{S^{\perp 2} + S^{z2}}$$

$$\vec{S}(\vec{r}) = (S^{\perp}\mathrm{Re}[e^{i\vec{k}\vec{r}}], S^{\perp}\mathrm{Im}[e^{i\vec{k}\vec{r}}], S^z) \quad, \quad \vec{k} = (\frac{4\pi}{3}, 0)$$

$$E_H^{mix} = -L^2 \vec{H} \cdot \vec{M} = -L^2 \vec{H} \cdot (0, 0, S^z) = -L^2 H_z S^z$$

$$E_J^{mix} = -J \sum_{<ij>} \vec{S}_i \cdot \vec{S}_j = -J \sum_{<ij>} (S_i^{\perp} S_j^{\perp} \cos \alpha_{ij}^{\perp} + S_i^z S_j^z) =$$

$$= -JL^2(-3S^{\perp 2} + 6S^{z2}) = -JL^2(-3(1 - S^{z2}) + 6S^{z2}) = -JL^2(9S^{z2} - 3)$$

$$E_D^{mix} = -D \sum_{<ij>} S_i^{\perp} S_j^{\perp} \sin \alpha_{ij}^{\perp} = ... = -DL^2 S^{\perp 2} 3\sqrt{3} = -3\sqrt{3}DL^2(1 - S^{z2})$$

$$E^{mix} = -L^2(H_z S^z + J(9S^{z2} - 3) + 3\sqrt{3}D(1 - S^{z2}))$$

$$\frac{\mathrm{d}E^{mix}}{\mathrm{d}S^z} = -L^2(H_z + 18JS^z - 6\sqrt{3}DS^z) = 0$$

$$S^z_{min} = \frac{H_z}{6\sqrt{3}D - 18J}$$

(3.10)

Since $S^z = M_z$, we can also compute the magnetic susceptibility. For $J = 1$:

$$\frac{1}{\chi} = \frac{H_z}{M_z} = \frac{H_z}{S^z} = 6\sqrt{3}D - 18 \approx 10.39D - 18 \qquad (3.11)$$

This result is consistent with the magnetic susceptibility measurement in Figure 3.15.

Most importantly, we have analytically explained why is the phase boundary without an external field at $D = \sqrt{3}$.

3.2   Finite-temperature properties

3.2.1   Heat capacity and critical temperature

Specific heat capacity was measured using the method described in subsection 2.3.4 for various D to observe the effect of DMI on critical ordering temperature.
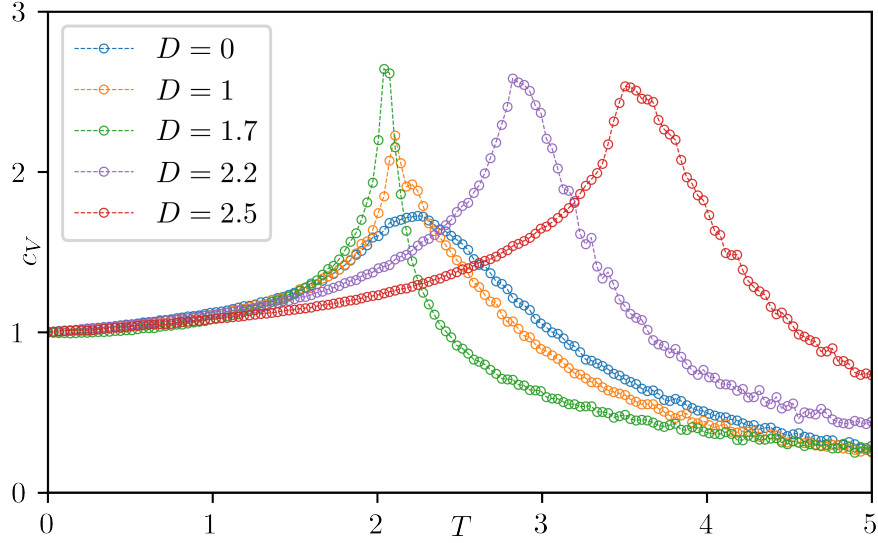
Figure 3.16: Specific heat capacity vs. temperature for various DMI strengths D.

Figure 3.16 shows specific heat capacities for $D = 0$, $D = 1$, $D = 1.7$ with ferromagnetic order and $D = 2.2$, $D = 2.5$ with antiferromagnetic order. Peaks of specific heat capacity at critical ordering temperature indicate a magnetic phase transition. For the ferromagnetic order ($D < \sqrt{3}$), the critical temperature does not change with D. The critical temperature of antiferromagnetic order ($D > \sqrt{3}$) significantly increases with increasing D. The temperature scale is defined with respect to the energy scale of the exchange interaction as described in Appendix A, meaning that $T = 157.9$ K ≈ 1 $k_B T/J$.

We can see a fundamental discrepancy in the model – specific heat capacity goes to 1 at zero temperature, while it should correctly go to zero. This is a property of the classical Heisenberg model (Kapitan et al. [2019]).

To determine the critical temperature more precisely, we will employ the method of Binder cumulants.
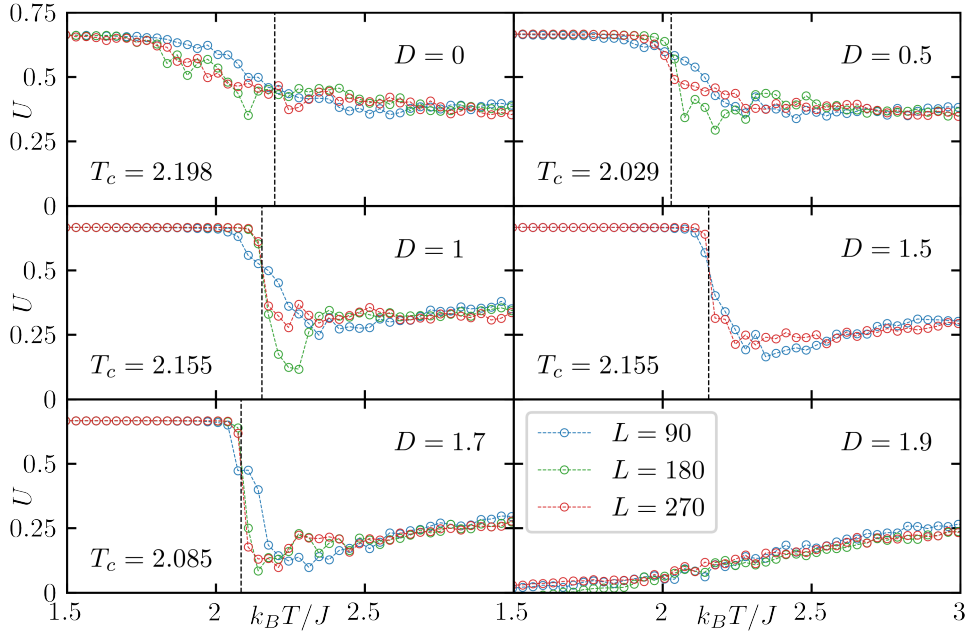
Figure 3.17: Binder cumulant U vs. temperature for $J = 1$, various D and lattice size L. The crossover of U curves for various lattice sizes indicates a phase transition. The critical temperature is marked by the vertical line.
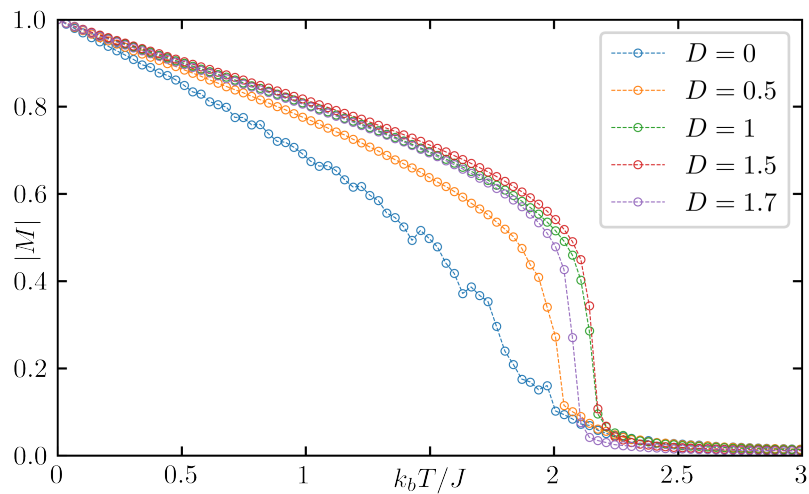

Figure 3.18: Magnetization vs. temperature for $J = 1$, various D and $L = 270$.
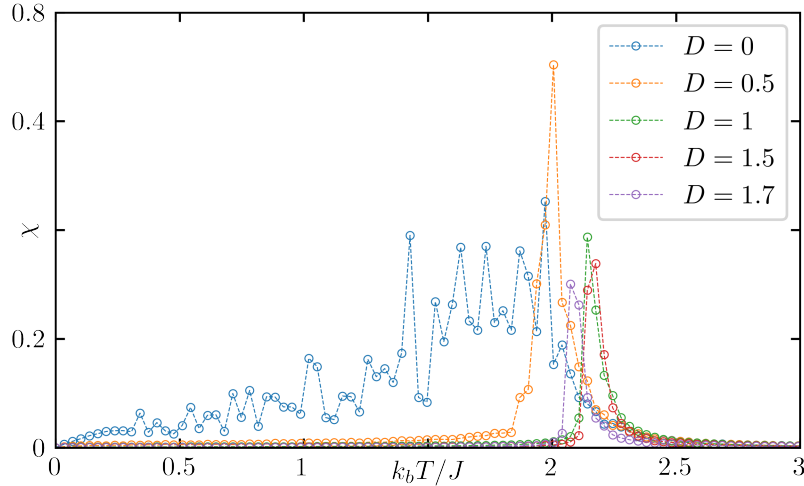
Figure 3.19: Magnetic susceptibility vs. temperature for $J = 1$, various D and $L = 270$.

Figure 3.17 shows the temperature dependence of Binder cumulant for various D and lattice sizes $L = 90$, $L = 180$ and $L = 270$. Critical temperature T_c was determined from the crossover point of different curves. The critical temperature is in the range of $2 < T_c < 2.2$ and does not show any trend on D. Crossover for $D = 1.9$ (antiferromagnetic phase) could not be determined.

Figure 3.18 shows the temperature dependence of magnetization for various ferromagnetic D, which qualitatively follows the standard ferromagnetic curve (Brillouin expression or Bloch's law). DMI visibly enhances magnetization at higher temperatures.

In Figure 3.19, we see that DMI reduces the magnetic susceptibility of the ferromagnetic phase at lower temperatures.

3.2.2 Magnetization

In zero-temperature measurements, the moment vectors in the ferromagnetic order ($J = 1$, $D < \sqrt{3}$) are completely collinear and $|\vec{M}| = 1$. Let us investigate the role of temperature – how do the thermal excitations, which are disordering the moments, lower the overall magnetization and what is the role of the DMI. Let us look at z-direction magnetization dependence on the external field in the out-of-plane direction for various temperatures and D.
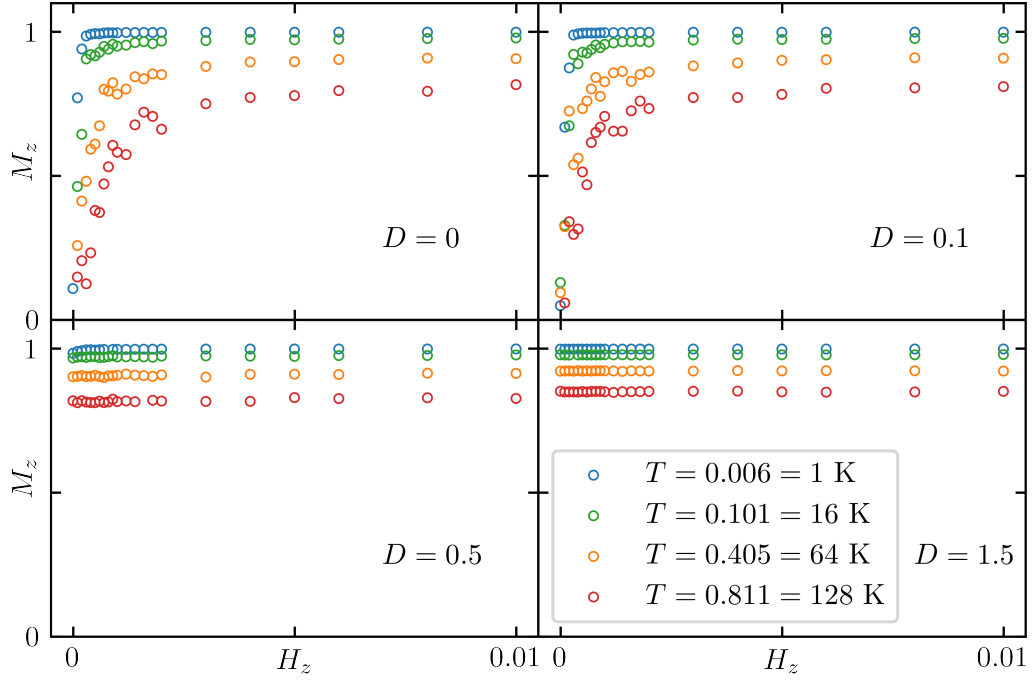
Figure 3.20: Magnetization in z-direction vs. external field in the out-of-plane direction for various temperatures and D. Grouped into subplots by D. $L = 180$.
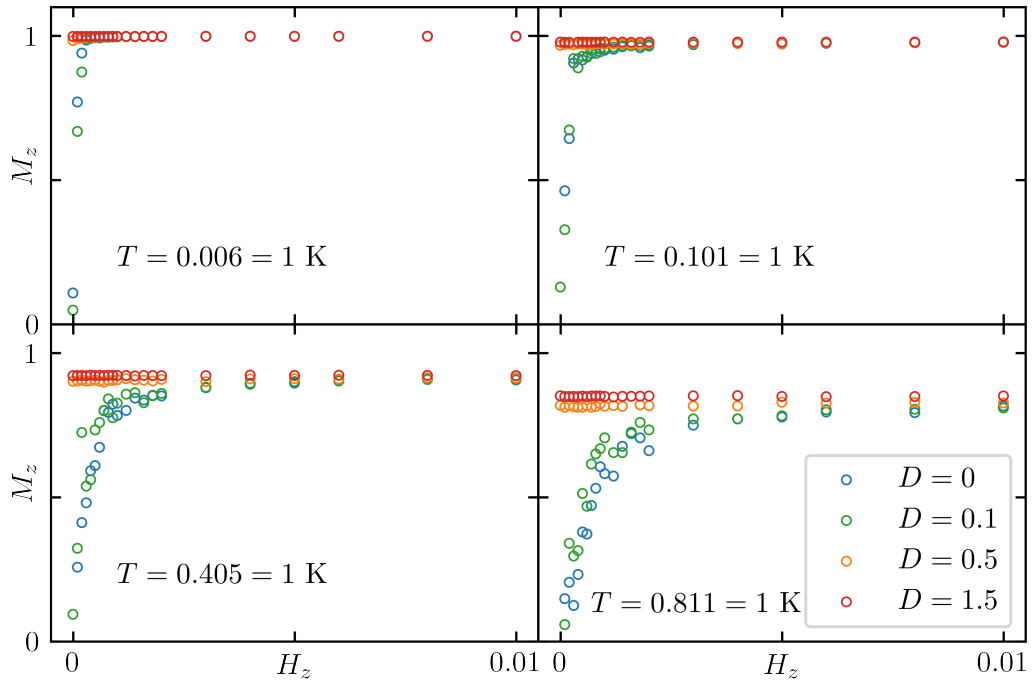

Figure 3.21: Magnetization in z-direction vs. external field in the out-of-plane direction for various temperatures and D. Grouped into subplots by temperature. $L = 180$.

In Figure 3.20, we see that for all values of D, higher temperature consistently lowers the magnetization in the z-direction in the whole range of H_z. The

38

magnetization present in a strong external field is less at higher temperatures, regardless of D. On the other hand, DMI significantly increases magnetization in the z-direction in the low external field. For $D = 0$ and small H_z, M_z is small – the magnetization direction of the ferromagnetic phase is fairly random. However, for larger values of D, magnetization in the z-direction is more favourable and the effect of the thermal disordering diminishes. Finally, for $D = 1.5$, the magnetization dependencies are constant. Despite that, DMI does increase magnetization in strong external fields.

The effect of DMI is better visible in Figure 3.21, where we clearly see the stabilization effect for weak external fields. This effect is more closely investigated in subsection 3.2.3 and subsection 3.3.2

3.2.3 Magnetization pinning

In the previous section, we noticed that the DMI affects the ferromagnetic phase in such a way that magnetization in the z-direction is favoured. In this section, we look at this effect from a different angle.

For a few selected D, we will repeatedly run simulations to find the ground state using the usual method described in subsection 2.3.1. We will then calculate the probability distribution of M_z depending on D. The external field is disabled in this experiment.
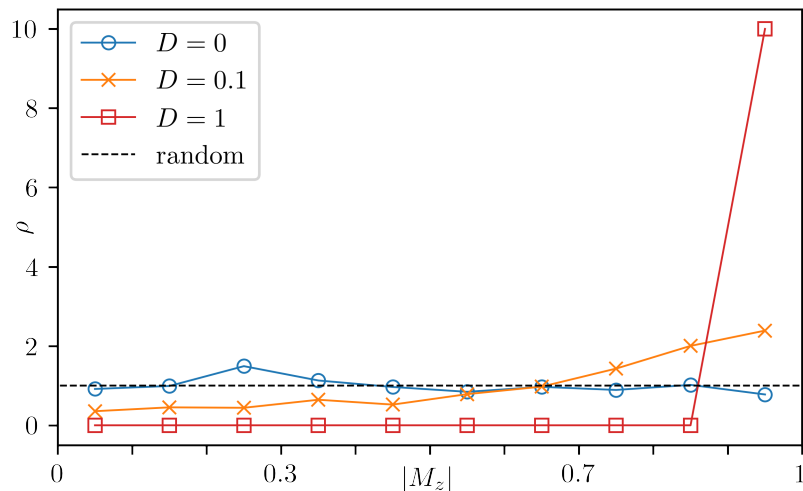

Figure 3.22: Probability distribution density of magnetization in z-direction for various D. The dashed line shows the distribution of M_z for $\vec{M}$ randomly distributed on a unit sphere. 300 samples for each D. $L = 180$.

In Figure 3.22, we see that for $D = 0$, the measured M_z distribution is roughly equal to the random distribution. For $D = 0.1$, we see that larger M_z are slightly favoured. For $D = 1$, all magnetization samples are $0.9 < M_z \leq 1$. The ferromagnetic phase strongly favours magnetization in the z-direction.

3.3 Hysteresis loop

In this section, we will present hysteresis loops calculated for various DMI strengths and temperatures. We will later see that temperature plays an important role and significantly affects the hysteresis loop calculated in this model. The hysteresis loop is calculated using the method described in subsection 2.3.5.

3.3.1 Zero-temperature hysteresis

We start with measuring the hysteresis loop at zero temperature. To be more precise, we set $T = 0.00006 = 0.01$ K, which is many orders of magnitude smaller than exchange interactions energies.
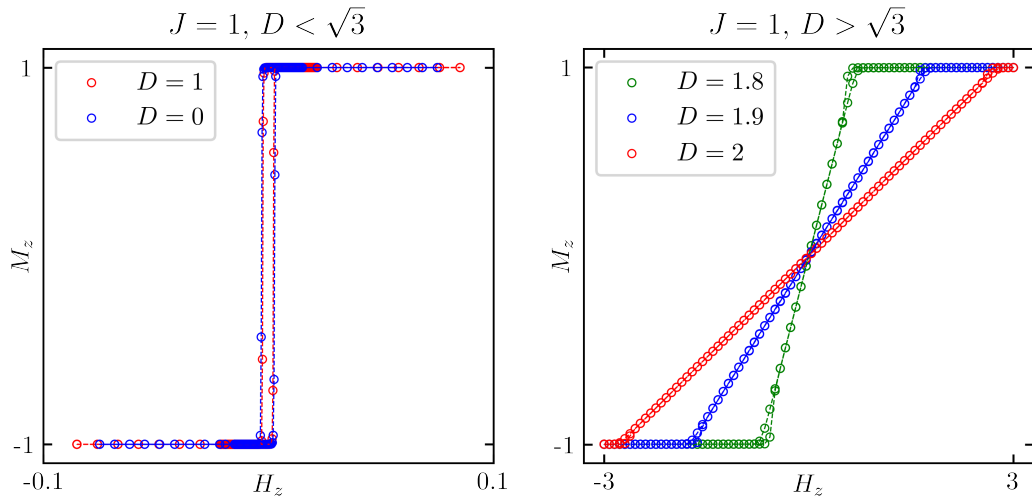

Figure 3.23: Hysteresis loop for $J = 1$ and various D in the out-of-plane direction. Left plot: ferromagnetic phase, right plot: antiferromagnetic phase. $L = 90$.

Figure 3.23 shows the hysteresis loop in the out-of-plane direction. In the left plot, we see a ferromagnetic behaviour without almost any hysteresis (coercivity $H_c \approx 0$, notice the small H_z scale). The very narrow gap in the hysteresis loop is a computational artifact caused by an imperfection of the spin dynamics method. In the case of a magnetization flip, the speed of the flip is proportional to the driving force of the external field. Thus, for field strength approaching zero, the number of time steps required to do a full magnetization flip goes to infinity. However, the computation needs to finish in a reasonable amount of time, so the number of time steps is limited, resulting in this artifact. The important fact is that D does not modify the hysteresis loop at zero temperature. DMI does not cause hysteresis for the ferromagnetic phase ($D < \sqrt{3}$) at zero temperature.

On the right side, we see a hysteresis loop for the antiferromagnetic phase ($D > \sqrt{3}$). Remanence $M_r = 0$ and coercivity $H_c = 0$, so no hysteresis was observed and the curve is fully consistent with the phase diagram observed in Figure 3.11.
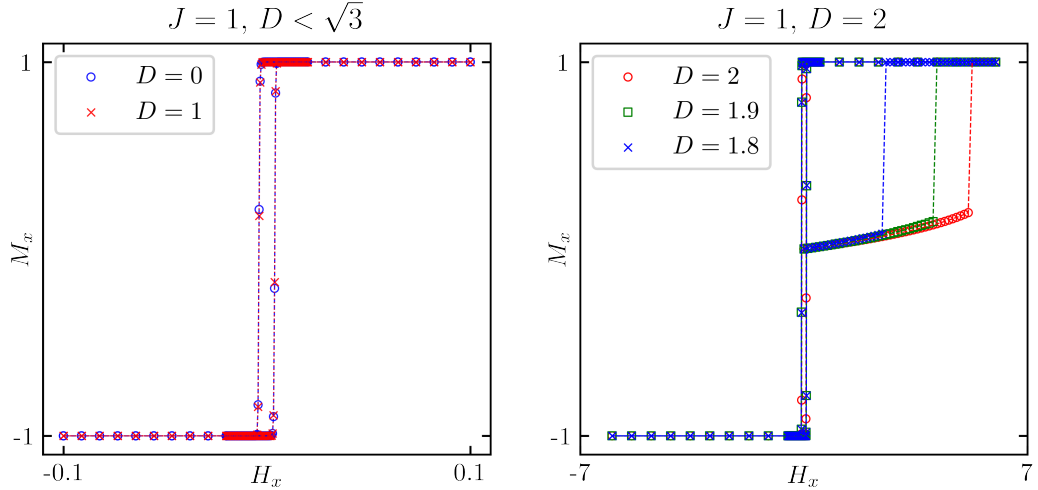
Figure 3.24: Hysteresis loop for $J = 1$ and various D in the in-plane direction. Left plot: ferromagnetic phase, right plot: antiferromagnetic phase, including the virgin curve. $L = 90$.

In the in-plane direction, the system behaves the same as in the out-of-plane direction for $D < \sqrt{3}$ – the ferromagnetic phase simply flips from $M_x = -1$ to $M_x = 1$.

However, for $D > \sqrt{3}$, the situation gets more complicated. In the plot for $D > \sqrt{3}$, the simulation begins with $H_x = 0$ and $M_x = 0$, first mapping the virgin curve up until magnetization saturation and then mapping out the rest of the hysteresis loop. In subsection 3.1.2, we have observed ferromagnetic and antiferromagnetic phases depending on D and H_x. In Figure 3.24, the magnetization $M_x \approx 0$ corresponds to the antiferromagnetic phase and $M_x = \pm 1$ to the ferromagnetic phase. We also see a sharp phase transition between the two phases in the hysteresis loop, ferromagnetic and antiferromagnetic phase (both phases are also present in the phase diagram in Figure 3.11). Due to hysteresis, the phase transitions happening in the hysteresis loop do not directly correspond to the phase boundary in the phase diagram! Take, for example, the case of $D = 2$: the phase boundary is located around $H_x = 1$ in the phase diagram, while the phase transition occurs at around $H_x = 5$ in the hysteresis loop. We need a larger external field to force the lattice to transition from the antiferromagnetic to the ferromagnetic phase.

However, once the lattice state is ferromagnetic, it does not go back to antiferromagnetic. Around $H_x = 0$, it just flips from $M_x = 1$ to $M_x = -1$, just like in the $D < \sqrt{3}$ case. This behaviour is altered at higher temperatures, where the lattice transitions back to antiferromagnetic around $H_x = 0$ (see section 3.3.2).

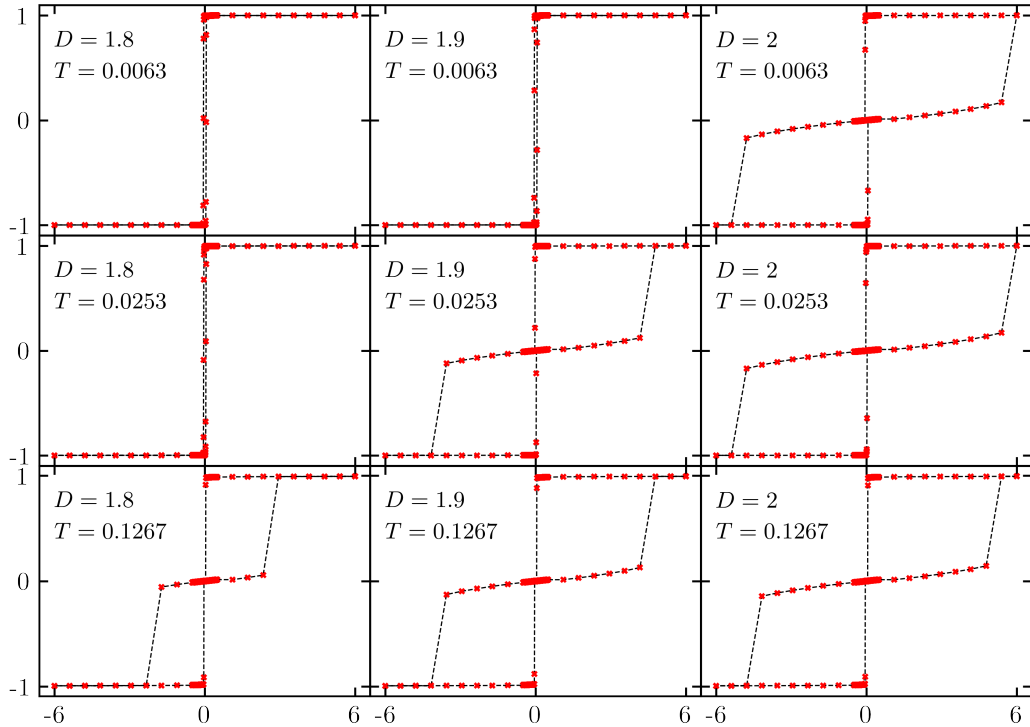### 3.3.2 Finite-temperature ferromagnet hysteresis

In-plane direction

Figure 3.25: Hysteresis loop of the ferromagnetic phase in the in-plane direction for various D and temperatures. Without the virgin curve. $L = 90$.

If we compare hysteresis loops in Figure 3.25 with Figure 3.24, we immediately see the effect of temperature on the system. For lower temperatures at $T = 0.0063$, systems with lower D behave the same as in zero temperature, flipping magnetization from $M_x = 1$ to $M_x = -1$ around $H_x = 0$ and staying in the ferromagnetic phase, even though the antiferromagnetic phase is more favourable around $H_x = 0$ (see Figure 3.11). At low temperatures, only systems with stronger D transition to the antiferromagnetic phase around $H_x = 0$. However, at higher temperatures, the transition is happening even for systems with smaller D.

One possible explanation is that the ferromagnetic phase forms a local energy minimum and at low temperatures, the system cannot overcome the energy barrier to get to the global energy minimum represented by the antiferromagnetic phase. Higher temperatures allow the system to overcome this barrier due to thermal fluctuations.
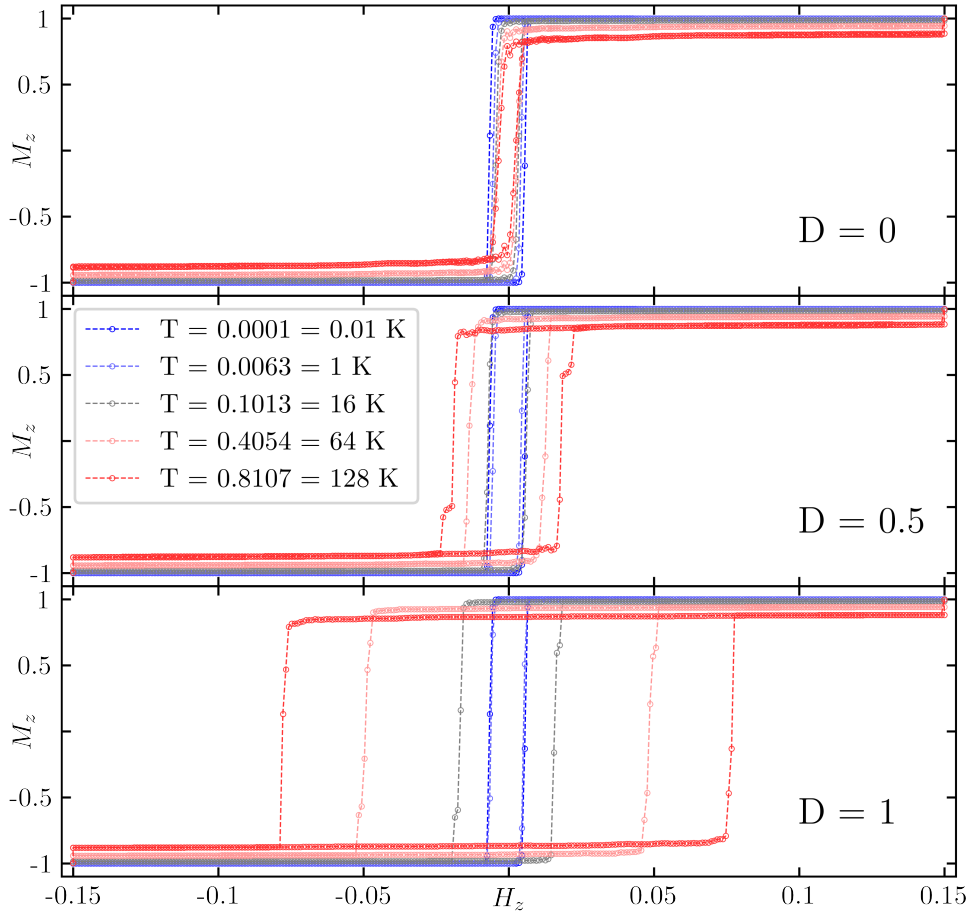
Out-of-plane direction

Figure 3.26: Hysteresis loop of the ferromagnetic phase in the out-of-plane direction for various D and temperature. $L = 90$.

Figure 3.26 shows the hysteresis loop for ferromagnetic phases for various D and temperature. As in the previous subsection, the very narrow hysteresis seen for low D and temperature is a computational artifact related to the fact that each simulation step has a finite amount of time steps, not enough to flip the magnetization and establish equilibrium in vanishingly small external fields. More importantly, though, the figure shows a hysteresis broadening caused by a combination of temperature and DMI. The significance of said hysteresis increases with increasing D and temperature and can be quantified by magnetic coercivity H_c – strength of the external magnetic field required to flip the z-magnetization of the system.

This temperature-induced hysteresis is further investigated in the following section.

3.4   Temperature and DMI induced hysteresis

In this section, we will investigate the hysteresis (and non-zero coercivity) shown in Figure 3.26. We will focus on a very narrow, but interesting part of the

hysteresis loop – the magnetization flip.

3.4.1   Simulation setup

To explore the magnetization flip, we need a frequent sampling of several observables, including snapshots of the whole lattice. Capturing such large amounts of data for the whole hysteresis loop is inefficient and unnecessary, because most of the time, the lattice is purely ferromagnetic. We are mainly interested in the dynamics of the magnetization flip.

We will perform a simulation of the magnetization flip using the spin dynamics method. Unlike previous simulations, the initial state will not be random, but all spins are set such that $\vec{S} = (0, 0, -1)$, such that $M_z = -1$ – an ideal ferromagnet. The external magnetic field is set to a constant value $\vec{H} = (0, 0, H_c)$, where H_c is the coercivity of the system for given D and temperature. The system is then simulated until the magnetization flip from $M_z = -1$ to $M_z = 1$ occurs (about 500 000 spin dynamics steps were sufficient). The average magnetization and energy of the system are sampled frequently during the simulation.

3.4.2   Energy barrier

First, let us see what is the development of the energy of the system during the magnetization flip. We will assume that the energy of the system is mainly determined by its magnetization M_z.
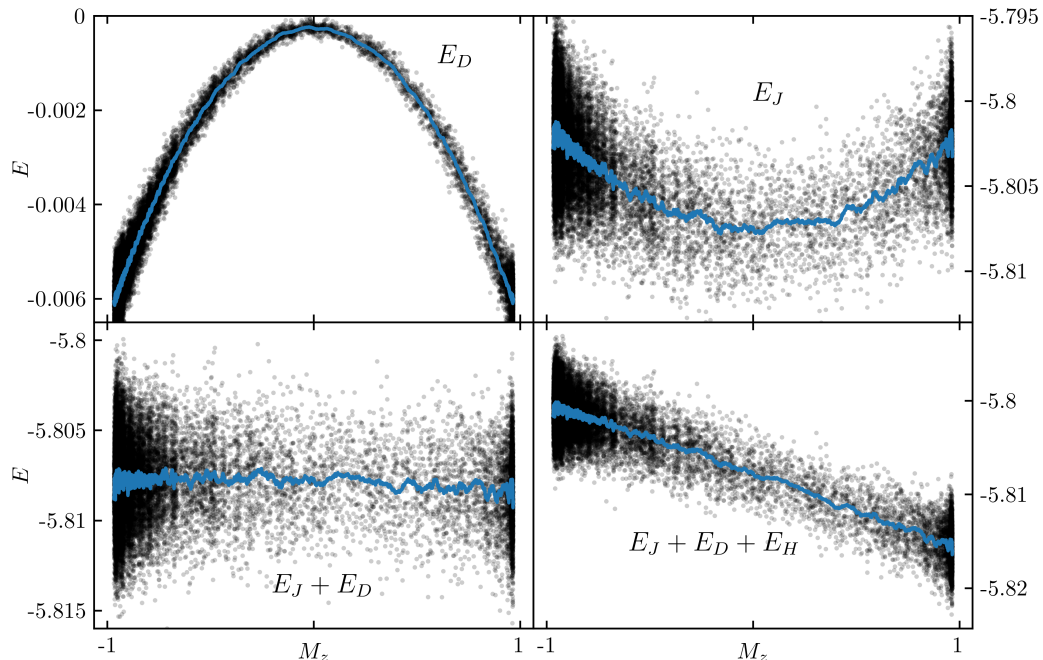

Figure 3.27: Energy of different interactions vs. magnetization during the magnetization flip. $D = 0.5$, $T = 0.203 = 32$ K, $H_z = 0.0074$, $L = 90$. Black dots represent individual measurements, blue line is smoothed average of 5 simulation runs.

Figure 3.27 shows energies of different interactions vs. magnetization in the z-

direction. The top-left plot shows the energy of the DMI. Several important facts are visible in this plot. Firstly, the assumption that energy depends mainly on magnetization is valid for the DMI – the individual measurements do not deviate far from the averaged curve. Secondly, E_D approaches zero for $M_z = 0$. Thirdly, the curve is parabolic, forming an energy barrier between $M_z = -1$ and $M_z = 1$. The top-right plot shows the exchange interaction energy. The measurement deviation is much larger in this case and the assumption that magnetization uniquely determines energy seems to be invalid here. The averaged curve seems to be parabolic, but in the negative energy direction, like it is compensating the energy E_D. That idea is confirmed in the left-bottom plot, which shows $E_J + E_D$. Indeed, E_D and E_J are compensated and $E_J + E_D$ is constant. The last plot in the bottom right corner shows the total energy of the system. Here, we see that the energy of the interaction with the external field dominates, forcing the system to flip its magnetization.

Figure 3.27 showed that a well-defined energy barrier caused by DMI exists. This barrier also explains why DMI favours ferromagnetic ground state in the z-direction, investigated in subsection 3.2.3.
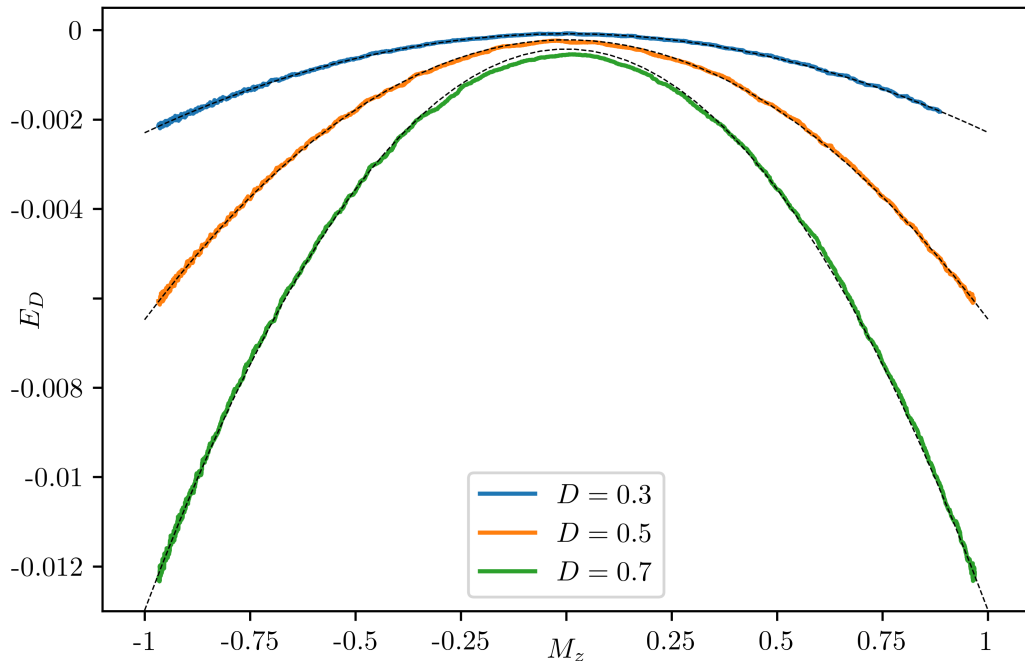

Figure 3.28: DMI energy vs. magnetization for various D. $T = 0.203 = 32$ K, $L = 90$. Average of 5 simulation runs. Dashed black lines show parabolic fit.

Figure 3.28 shows the DMI energy for various D. We see that the energy barrier height increases with increasing D, but the shape continues to be parabolic.
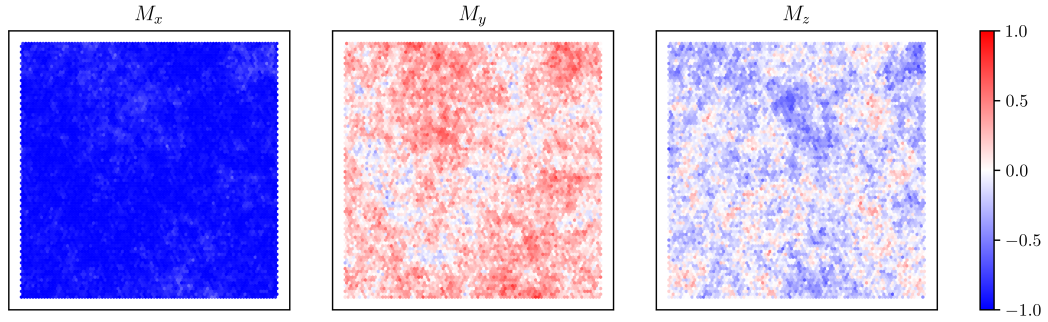
Figure 3.29: Lattice state in the middle of magnetization flip. $D = 0.3$, $T = 0.203 = 32$ K, $H_z = 0.007$, $L = 90$.

Figure 3.29 shows a lattice state in the middle of the magnetization flip for $D = 0.3$, which is not too strong. Notice that the lattice is homogeneous to a large extent.
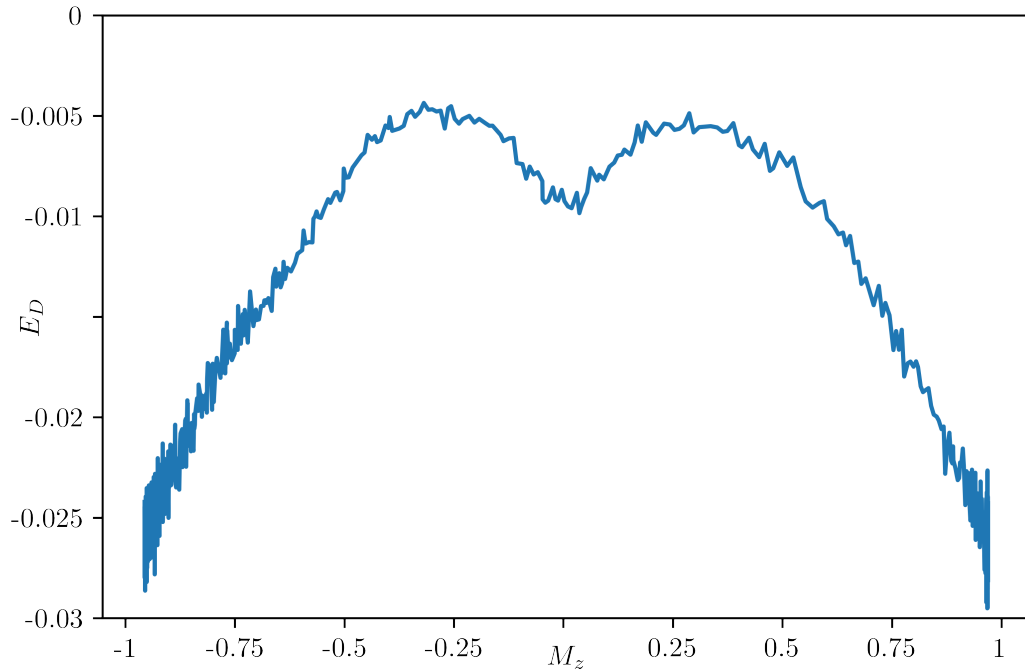

Figure 3.30: DMI energy vs. magnetization for $D = 1$. A single simulation run. $L = 90$.

Figure 3.30 again shows the DMI energy vs magnetization for a stronger $D = 1$. In contrast with Figure 3.28, the parabolic shape of the energy dependence is broken. This is caused by inhomogenities in the finite system. Note that this is only one of many examples and the shape of the curve is not generally symmetric nor does it have exactly two maxima.
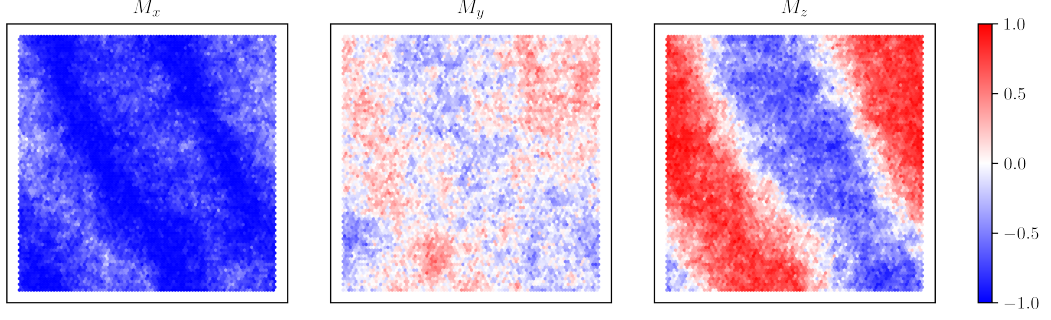
Figure 3.31: Lattice state in the middle of magnetization flip. $D = 1$, $T = 0.203 = 32$ K, $H_z = 0.04$, $L = 90$.

Figure 3.31 shows a lattice state in the middle of the magnetization flip for stronger $D = 1$. Contrary to Figure 3.29, the lattice is not homogeneous and magnetization domains emerge.

Energy barrier size

Let us now focus on the energy barrier caused by DMI and its height, which will be calculated as

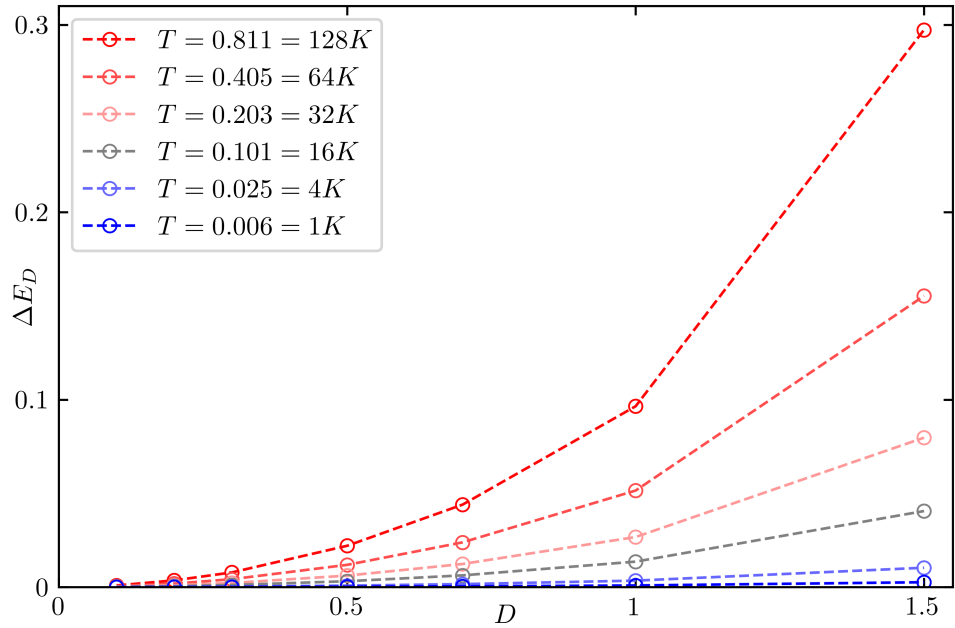$$\Delta E_D = E_D(M_z = 0) - E_D(M_z = -1) \tag{3.12}$$

Figure 3.32: DMI energy barrier height vs. D at various temperatures.

Figure 3.32 shows dependence of ΔE_D on D at various temperatures. We see that the ΔE_D non-linearly increases with D at all temperatures.

47
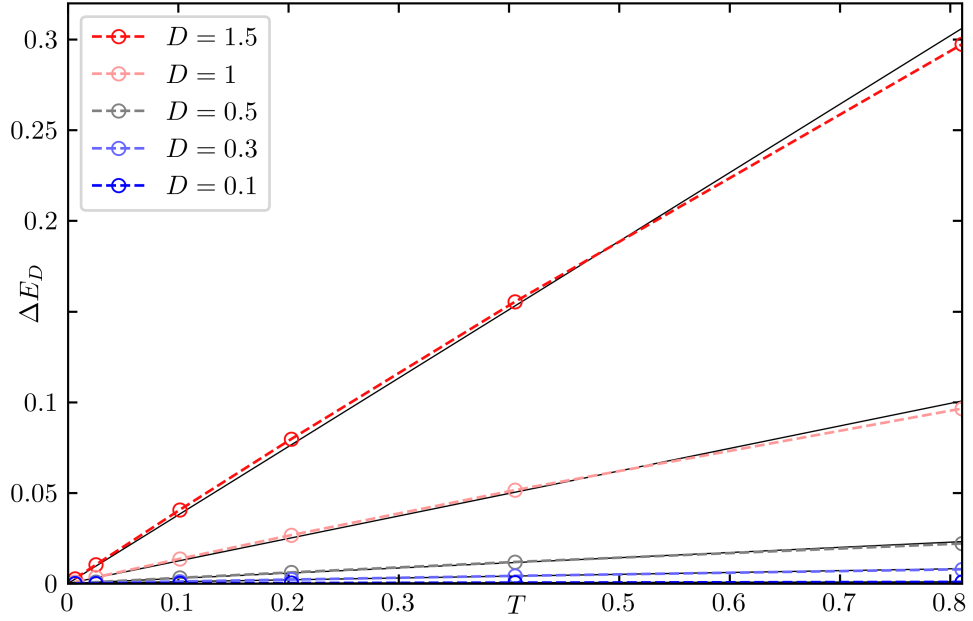
Figure 3.33: DMI energy barrier vs. temperature for various D. Black lines show linear fits of the individual curves.

Figure 3.32 shows dependence of ΔE_D on temperature for various D. ΔE_D linearly increases with temperature with high precision.

Energy barrier vs. coercivity

Figure 3.34: Observed DMI energy barrier height ΔE_D vs. coercivity H_c.

We have analyzed the DMI energy barrier during the magnetization flip. Figure 3.34 compares the coercivity H_c in the hysteresis loop (Figure 3.26) and the energy barrier height ΔE_D calculated for equal D and temperatures. It verifies that the barrier height is indeed equal to coercivity (in units of energy). This is

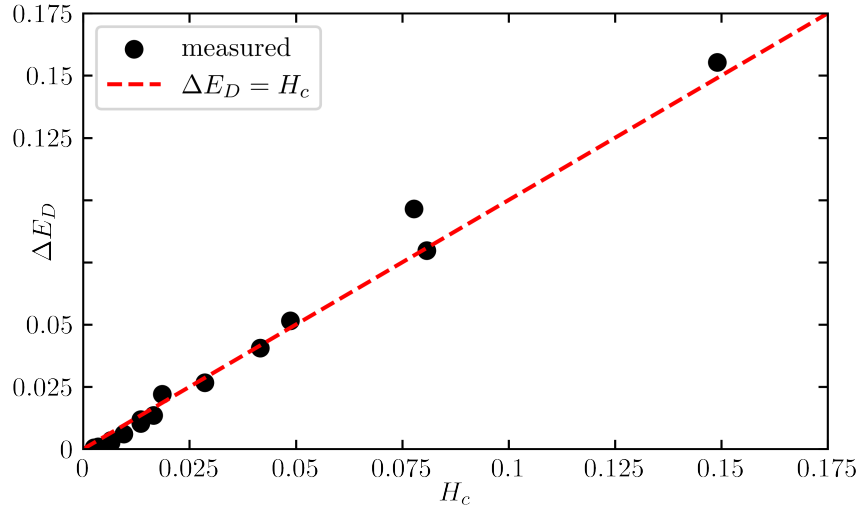another indication that the system behaves as expected – it is following the gradient of the magnetization-dependent energy. Most importantly, the hysteresis observed in Figure 3.26 can be satisfyingly explained by the energy barrier.

3.4.3 Observed partial antiferromagnetic ordering

In the last section, we observed the energy barrier induced by the negative energy of the DMI. However, we do not know anything about the exact lattice configuration leading to this energy decrease. Let us look at the lattice configuration before the magnetization flip when the lattice finds itself in the DMI energy well.
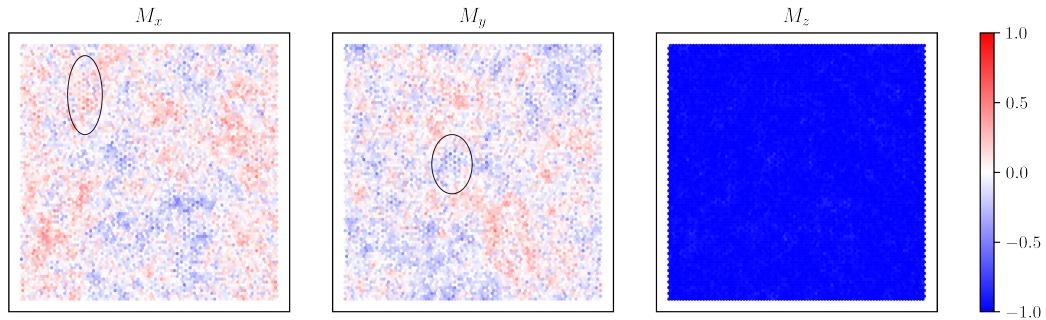
Figure 3.35: Lattice state of ferromagnetic phase $M_z \approx -1$ for $D = 1.7$, $T = 0.101 = 16$ K, $L = 90$. Traces of the antiferromagnetic phase are visible in the marked areas.

Figure 3.35 shows the lattice state of the ferromagnetic phase for a very strong $D = 1.7$. We can see traces of short-range antiferromagnetic ordering, similar to that seen in Figure 3.3.
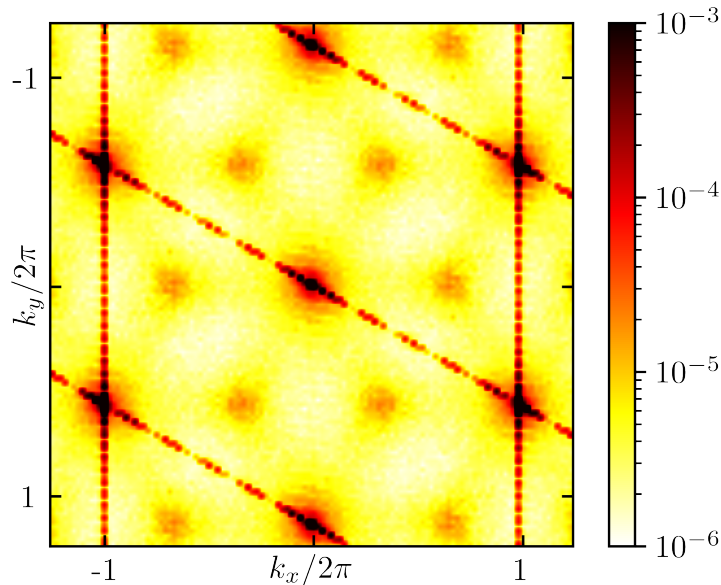
Figure 3.36: Structure factor of ferromagnetic phase $M_z \approx -1$ for $D = 1.7$, $T = 0.101 = 16$ K. Displayed in logarithmic scale.

Figure 3.36 shows the structure factor of that lattice state. Peak at $\vec{k} = (0,0)$ and peaks at $|\vec{k}| = \frac{4\pi}{\sqrt{3}}$ are by far the most significant. These peaks belong to the ferromagnetic phase. However, a set of weaker peaks at $|\vec{k}| = \frac{4\pi}{3}$ is also visible, although these peaks are orders of magnitude smaller. These peaks belong to the cycloidal antiferromagnetic phase introduced in section 3.1.

Figure 3.36 clearly shows that a small trace of the antiferromagnetic phase exists in the mainly ferromagnetic phase at higher temperatures and with strong DMI.

Moreover, the antiferromagnetic phase can explain the negative DMI energy E_D. Let us recall the analytical computations of antiferromagnetic phase energy in subsection 3.1.3 which arrived at the result $E_D^{\text{AFM}} = -3\sqrt{3}DL^2$ – the energy of DMI is negative in the antiferromagnetic phase.

Conclusion

In this thesis, we investigated the effect of out-of-plane Dzyaloshinskii-Moriya interaction (DMI) between nearest neighbours on magnetic ordering of the classical Heisenberg model on a two-dimensional triangular lattice. Apart from DMI, ferromagnetic exchange interaction between nearest neighbours and interaction with external field were present. We used Markov Chain Monte Carlo and spin dynamics method to calculate, among other results, the ground state, heat capacity and hysteresis loop for various model parameter combinations. Varied parameters included: DMI strength, in-plane/out-of-plane external magnetic field strength and temperature.

We constructed two magnetic phase diagrams parametrized by external magnetic field strength and DMI strength: one for out-of-plane external field and one for in-plane external field. Three different magnetic orderings have been observed: ferromagnetic ordering for weak DMI, antiferromagnetic ordering for $D/J > \sqrt{3}$ and a mixture of the former two. The antiferromagnetic ordering is a cycloidal one, with spins lying completely in the lattice plane, neighbouring spins forming an angle of 120 ° with propagation vector $\vec{k} = (1/3, 1/3)$. The mixed state is induced by the out-of-plane external field. It is a conical magnetic ordering, with z-component of the spins forming a ferromagnetic order and xy-component forming the cycloidal antiferromagnetic order. In the in-plane phase diagram, a first-order phase transition occurs on the phase boundary. In the out-of-plane case, a second-order phase transition occurs. The observed phase diagram has been supported by analytical calculations.

We found that DMI affects the finite-temperature properties of the ferromagnetic phase, in that it favours magnetization in the z-direction. Furthermore, it enhances magnetization at higher temperatures, although the critical temperature T_c seems not to be affected by DMI.

No chiral magnetism, such as skyrmions, or spin spirals has been observed, rather being a domain of in-plane DMI.

Finite-temperature hysteresis loop calculations of ferromagnetic phase ($D < \sqrt{3}$) have found non-zero coercivity, which linearly depends on temperature and increases even more rapidly with DMI strength. Analysis of the energetics of the magnetization flip in the hysteresis loop has uncovered that the hysteresis is caused by DMI energy barrier in parabolic shape (when plotted against z-direction magnetization). One possible mechanism for this has been observed for especially strong $D = 1.7$ – traces of antiferromagnetic cycloidal order have been found in the otherwise ferromagnetic phase. These traces lower the DMI energy. However, many questions about this phenomenon are left unanswered. Why is there no decrease in DMI energy at $M_z = 0$? How to explain the peculiar linear temperature dependence? The exact nature of the spin arrangement that decreases DMI energy and creates the energy barrier is yet unknown and it is an interesting subject which could be further studied in the future. Another question left unanswered because of lack of time is whether this effect can be observed in other models, such as the quantum Heisenberg model, or whether it is a property of the classical Heisenberg model.

The results obtained in this thesis, mainly the magnetization curves and

hysteresis loops, were compared with yet unpublished experimental data for $EuAl_{12}O_{19}$ compound measured by Gaël Bastien, Ph. D. [1]. However, theoretical and experimental data do not match and the model in this thesis is not suitable to describe magnetic properties of the compound.

[1]Charles University, Faculty of Mathematics and Physics, Department of Condensed Matter Physics, Prague, Czech Republic

Bibliography

Amal Aldarawsheh, Moritz Sallermann, Muayad Abusaa, and Samir Lounis. A spin model for intrinsic antiferromagnetic skyrmions on a triangular lattice, 2023.

N.W. Ashcroft and N.D. Mermin. *Solid State Physics*. Cengage Learning, 2011. ISBN 9788131500521.

Federico Becca and Sandro Sorella. *Quantum Monte Carlo Approaches for Correlated Systems*. Cambridge University Press, 2017. doi: 10.1017/9781316417041.

Ka Chan, C. Lenard, and Terence Mills. An introduction to markov chains. 12 2012. doi: 10.13140/2.1.1833.8248.

Albert Fert, Vincent Cros, and Joao Sampaio. Skyrmions on the track. *Nature nanotechnology*, 8(3):152–156, 2013.

N. A. Fortune, Q. Huang, T. Hong, J. Ma, E. S. Choi, S. T. Hannahs, Z. Y. Zhao, X. F. Sun, Y. Takano, and H. D. Zhou. Evolution of magnetic field induced ordering in the layered quantum heisenberg triangular-lattice antiferromagnet $ba_3cosb_2o_9$. *Phys. Rev. B*, 103:184425, May 2021. doi: 10.1103/PhysRevB.103.184425. URL https://link.aps.org/doi/10.1103/PhysRevB.103.184425.

Woo Seung Ham, Abdul-Muizz Pradipto, Kay Yakushiji, Kwangsu Kim, Sonny H. Rhim, Kohji Nakamura, Yoichi Shiota, Sanghoon Kim, and Teruo Ono. Dzyaloshinskii–moriya interaction in noncentrosymmetric superlattices. *npj Computational Materials*, 7(1):129, Aug 2021. ISSN 2057-3960. doi: 10.1038/s41524-021-00592-8. URL https://doi.org/10.1038/s41524-021-00592-8.

Charles R. Harris, K. Jarrod Millman, Stéfan J. van der Walt, Ralf Gommers, Pauli Virtanen, David Cournapeau, Eric Wieser, Julian Taylor, Sebastian Berg, Nathaniel J. Smith, Robert Kern, Matti Picus, Stephan Hoyer, Marten H. van Kerkwijk, Matthew Brett, Allan Haldane, Jaime Fernández del Río, Mark Wiebe, Pearu Peterson, Pierre Gérard-Marchant, Kevin Sheppard, Tyler Reddy, Warren Weckesser, Hameer Abbasi, Christoph Gohlke, and Travis E. Oliphant. Array programming with NumPy. *Nature*, 585 (7825):357–362, September 2020. doi: 10.1038/s41586-020-2649-2. URL https://doi.org/10.1038/s41586-020-2649-2.

Sahbi El Hog, Ildus F. Sharafullin, H.T. Diep, H. Garbouj, M. Debbichi, and M. Said. Frustrated antiferromagnetic triangular lattice with dzyaloshinskii–moriya interaction: Ground states, spin waves, skyrmion crystal, phase transition. *Journal of Magnetism and Magnetic Materials*, 563:169920, dec 2022. doi: 10.1016/j.jmmm.2022.169920. URL https://doi.org/10.1016%2Fj.jmmm.2022.169920.

I. A. Iakovlev, O. M. Sotnikov, and V. V. Mazurenko. Bimeron nanoconfined design. *Phys. Rev. B*, 97:184415, May 2018a. doi: 10.1103/PhysRevB.97.184415. URL https://link.aps.org/doi/10.1103/PhysRevB.97.184415.

I. A. Iakovlev, O. M. Sotnikov, and V. V. Mazurenko. Supervised learning approach for recognizing magnetic skyrmion phases. *Phys. Rev. B*, 98:174411, Nov 2018b. doi: 10.1103/PhysRevB.98.174411. URL `https://link.aps.org/doi/10.1103/PhysRevB.98.174411`.

Anubhav Jain, Shyue Ping Ong, Geoffroy Hautier, Wei Chen, William Davidson Richards, Stephen Dacek, Shreyas Cholia, Dan Gunter, David Skinner, Gerbrand Ceder, and Kristin A. Persson. Commentary: The Materials Project: A materials genome approach to accelerating materials innovation. *APL Materials*, 1(1), 07 2013. ISSN 2166-532X. doi: 10.1063/1.4812323. URL `https://doi.org/10.1063/1.4812323`. 011002.

Vitalii Kapitan, Yuriy Shevchenko, Alexander Perzhu, and Egor Vasiliev. Thermodynamic properties of heisenberg spin systems. *Key Engineering Materials*, 806:142–154, 06 2019. doi: 10.4028/www.scientific.net/KEM.806.142.

M. Lakshmanan. The fascinating world of the landau–lifshitz–gilbert equation: an overview. *Philosophical Transactions of the Royal Society A: Mathematical, Physical and Engineering Sciences*, 369(1939):1280–1300, mar 2011. doi: 10.1098/rsta.2010.0319. URL `https://doi.org/10.1098%2Frsta.2010.0319`.

David P. Landau and Kurt Binder. *A Guide to Monte Carlo Simulations in Statistical Physics*. Cambridge University Press, 3 edition, 2009. doi: 10.1017/CBO9780511994944.

L. Landau and E. Lifshitz. 3 - on the theory of the dispersion of magnetic permeability in ferromagnetic bodies. reprinted from physikalische zeitschrift der sowjetunion 8, part 2, 153, 1935. In L.P. Pitaevski, editor, *Perspectives in Theoretical Physics*, pages 51–65. Pergamon, Amsterdam, 1992. ISBN 978-0-08-036364-6. doi: https://doi.org/10.1016/B978-0-08-036364-6.50008-9. URL `https://www.sciencedirect.com/science/article/pii/B9780080363646500089`.

J. Leliaert, J. Mulkers, J. De Clercq, A. Coene, M. Dvornik, and B. Van Waeyenberge. Adaptively time stepping the stochastic Landau-Lifshitz-Gilbert equation at nonzero temperature: Implementation and validation in MuMax3. *AIP Advances*, 7(12), 12 2017. ISSN 2158-3226. doi: 10.1063/1.5003957. URL `https://doi.org/10.1063/1.5003957`. 125010.

D. Loison, C. L. Qin, K. D. Schotte, and X. F. Jin. Canonical local algorithms for spin systems: heat bath and hasting?s methods. *The European Physical Journal B*, 41(3):395–412, oct 2004. doi: 10.1140/epjb/e2004-00332-5. URL `https://doi.org/10.1140%2Fepjb%2Fe2004-00332-5`.

Y Miyatake, M Yamamoto, J J Kim, M Toyonaga, and O Nagai. On the implementation of the 'heat bath' algorithms for monte carlo simulations of classical heisenberg spin systems. *Journal of Physics C: Solid State Physics*, 19(14):2539, may 1986. doi: 10.1088/0022-3719/19/14/020. URL `https://dx.doi.org/10.1088/0022-3719/19/14/020`.

Tôru Moriya. Anisotropic superexchange interaction and weak ferromagnetism. *Phys. Rev.*, 120:91–98, Oct 1960. doi: 10.1103/PhysRev.120.91. URL `https://link.aps.org/doi/10.1103/PhysRev.120.91`.

S. Muehlbauer, B. Binz, F. Jonietz, C. Pfleiderer, A. Rosch, A. Neubauer, R. Georgii, and P. Boeni. Skyrmion lattice in a chiral magnet. *Science*, 323(5916):915–919, feb 2009. doi: 10.1126/science.1166767. URL `https://doi.org/10.1126%2Fscience.1166767`.

Masamichi Nishino, Ismail Enes Uysal, Taichi Hinokihara, and Seiji Miyashita. Dynamical aspects of magnetization reversal in the neodymium permanent magnet by a stochastic landau-lifshitz-gilbert simulation at finite temperature: Real-time dynamics and quantitative estimation of coercive force. *Phys. Rev. B*, 102:020413, Jul 2020. doi: 10.1103/PhysRevB.102.020413. URL `https://link.aps.org/doi/10.1103/PhysRevB.102.020413`.

Eva Pavarini, E. Koch, Frithjof Anders, and and (eds. *Correlated Electrons: From Models to Materials.* 09 2012. ISBN 978-3-89336-796-2.

V. Sechovský. Magnetism in solids: General introduction. In K.H. Jürgen Buschow, Robert W. Cahn, Merton C. Flemings, Bernhard Ilschner, Edward J. Kramer, Subhash Mahajan, and Patrick Veyssière, editors, *Encyclopedia of Materials: Science and Technology*, pages 5018–5032. Elsevier, Oxford, 2001. ISBN 978-0-08-043152-9. doi: https://doi.org/10.1016/B0-08-043152-6/00872-X. URL `https://www.sciencedirect.com/science/article/pii/B008043152600872X`.

I. A. Sergienko and E. Dagotto. Role of the dzyaloshinskii-moriya interaction in multiferroic perovskites. *Physical Review B*, 73(9), mar 2006. doi: 10.1103/physrevb.73.094434. URL `https://doi.org/10.1103%2Fphysrevb.73.094434`.

B Skubic, J Hellsvik, L Nordström, and O Eriksson. A method for atomistic spin dynamics simulations: implementation and examples. *Journal of Physics: Condensed Matter*, 20(31):315203, jul 2008. doi: 10.1088/0953-8984/20/31/315203. URL `https://dx.doi.org/10.1088/0953-8984/20/31/315203`.

Kyung Mee Song, Jae-Seung Jeong, Biao Pan, Xichao Zhang, Jing Xia, Sunkyung Cha, Tae-Eon Park, Kwangsu Kim, Simone Finizio, Joerg Raabe, et al. Skyrmion-based artificial synapses for neuromorphic computing. *Nature Electronics*, 3(3):148–155, 2020.

A. Units of measurement

We use a single arbitrary energy scale for all interactions to simplify presentation of results. However, one needs to use real units of measurements when configuring UppASD. The exchange and Dzyaloshinskii-Moriya interaction strength must be specified in millirydbergs (mRy). The external field strength is entered in Teslas (T), temperature in Kelvins (K) and magnetic dipole moment in Bohr magnetons (μ_{B}).

Therefore, we need to convert these units when configuring an experiment or processing measured data. In all experiments, we fix the magnetic dipole moment to 1 μ_{B}.

Exchange interaction of 1 mRy is converted to external field Tesla equivalent according to following formula:

$$
\begin{aligned}
1 \text{ mRy} &\sim 2.17987 \cdot 10^{-21} \text{ J} \\
&\sim (2.17987 \cdot 10^{-21} \text{ J})/(9.27401 \cdot 10^{-24} \text{ J/T}) \cdot 1 \ \mu_{\mathrm{B}} \qquad \text{(A.1)} \\
&\sim 235.0314 \text{ T} \cdot 1 \ \mu_{\mathrm{B}}
\end{aligned}
$$

We can also convert Kelvins to the common energy scale in mRy:

$$
\begin{aligned}
1 \text{ mRy} &\sim 2.17987 \cdot 10^{-21} \text{ J} \\
&\sim (2.17987 \cdot 10^{-21} \text{ J})/(1.38065 \cdot 10^{-23} \text{ J/K}) \cdot 1 \ \mathrm{k_B} \qquad \text{(A.2)} \\
&\sim 157.8872 \text{ K} \cdot 1 \ \mathrm{k_B}
\end{aligned}
$$

B. Contribution to UppASD

UppASD was used extensively in this thesis. While using UppASD, we found a bug in its implementation of the heat bath method.

The bug is well visible in a simulation conducted by the thesis supervisor, Pavel Baláž. The simulation data are presented here with his permission.

The simulation is classical Heisenberg model of a two-dimensional square lattice with direct exchange interactions and in-plane DMI between nearest neighbours and external magnetic field applied in the out-of-plane direction. The model was used to construct low-temperature phase diagrams featuring magnetization and topological charge depending on DMI strength D and external field B. The low-temperature states were obtained via simulated annealing with two MCMC methods: either Metropolis-Hastings or heat bath method.
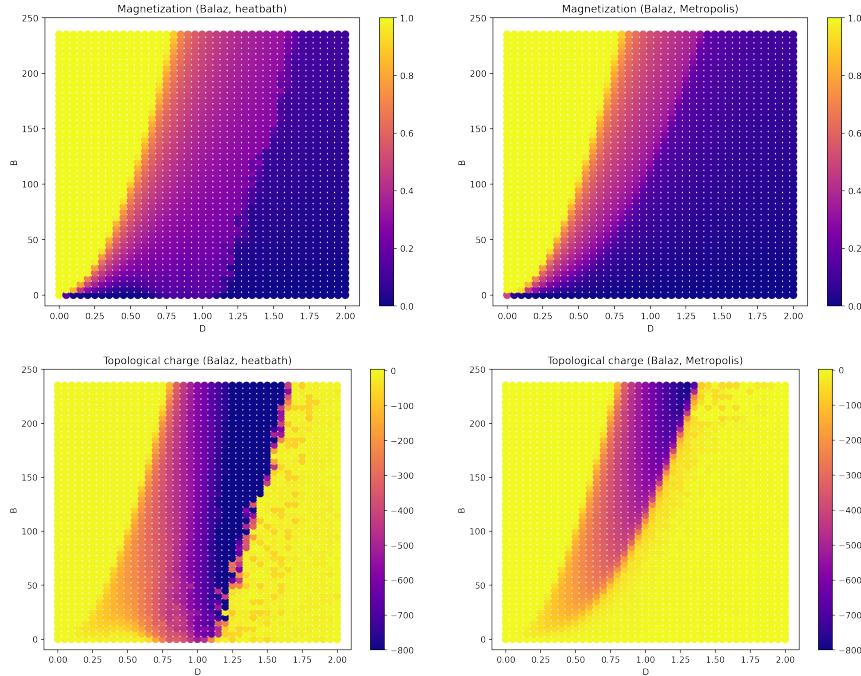

Figure B.1: Phase diagrams featuring magnetization and topological charge depending on DMI strength D and external magnetic field B calculated using either heat bath or Metropolis-Hastings method.

In Figure B.1, we see that heat bath and Metropolis-Hastings methods produce significantly different results. The Metropolis-Hastings phase diagrams are consistent with results presented in (Iakovlev et al. [2018a], Iakovlev et al. [2018b]). That suggests there is a bug in the heat bath implementation in UppASD.

We found a bug in the UppASD code related to random sampling in the heat bath method (the part that corresponds to Equation 1.24) and proposed a patch [1]. We then successfully verified that the patch resolves the issue – heat bath phase diagram matched the Metropolis-Hastings phase diagram.

---

[1]The patch is available online at `https://github.com/janpriessnitz/UppASD/commit/43c8f52a16e1f7ab78a06bcf76571e4dade2cff0`